Temperature analysis of hadronic current simulations using relativistic hydrodynamics for heavy-ion collisions scenarios

Author: Darío Chaires Arciniega

Advisor: Francico Shidartha Guzmán Murillo

Thesisho for a Master's degree in

Engineering Physics

Faculty of Physics and Mathematics

Universidad Michoacana de San Nicolás de Hidalgo

Morelia, Michoacán, México

October , 2025

To the significant ones who have transcended physical boundaries
and still have an immaterial yet well-established place in our hearts,
in the state of memories...

Acknowledgments

I thank Francisco Guzmán, for his patience and constant advisement; Iván Álvarez, for introducing me as a user to his improved Hydro code; and the whole group *5to estado de la materia* for all your discussion sessions and overall help.

Contents

ABSTRACT

This thesis investigates the application of relativistic ideal hydrodynamics to simulate the early-stage evolution of Quark-Gluon Plasma (QGP) in heavy-ion collisions (HIC). The study aims to test the feasibility of using an ideal fluid approximation—neglecting viscosity and employing a simple equation of state (EoS) to describe the thermodynamic and hydrodynamic properties of QGP, a deconfined state of matter theorized to mimic conditions of the early universe. The work leverages the CAFE code, a relativistic hydrodynamic solver, adapted to HIC scenarios by implementing Monte Carlo Glauber initial conditions and interpolating energy density profiles from the ECHO-QGP framework.
Keywords: *Quark-Gluon Plasma; Finite Volume Method; Conservative variables, Primitive variables; Impact parameter; Collision energy.*

RESUMEN

Esta tesis investiga la aplicación de la hidrodinámica ideal relativista para simular la evolución temprana del plasma de quarks-gluones (QGP) en colisiones de iones pesados. El estudio busca evaluar la viabilidad de usar una aproximación de fluido ideal despreciando la viscosidad y empleando una ecuación de estado simple para describir las propiedades termodinámicas e hidrodinámicas del QGP, un estado desconfinado de la materia que se teoriza para imitar las condiciones del universo primitivo. El trabajo utiliza el código CAFE, un solucionador hidrodinámico relativista, adaptado a escenarios de colisiones de iones pesados mediante la implementación de las condiciones iniciales de Monte Carlo Glauber y la interpolación de perfiles de densidad de energía del marco ECHO-QGP.
Palabras clave: *Plasma de quarks y gluones; Método de volumen finito; Variables*

conservativas, Variables primitivas; Parámetros de impacto; Energía de colisión.

1 Introduction

Throughout the history of modern humans, questions about the origin of what we perceive as the universe have arisen, independently of the culture and geographic position; many theories have been constructed with the main goal of answering the former existential query and, in the best of cases, obtain a satisfactory understanding. This work however, doesn't aim to answer, let alone fully understand the nature of such great inquiries, in fact, this work is intended to introduce and encourage concerned fellow contemporary researchers to one of the most powerful topics humanity has developed to describe early stages of the universe: Heavy-ion Collisions. This document has a strong basis for ideal hydrodynamics since it has proven to be a simple yet powerful introductory tool.

One of the important results from Heavy-Ion Collision experiments was detecting a new state of matter: the Quark-Gluon Plasma. This phenomenon was theorized in the late 1970s, and the word *plasma* was used indicating the presence of free color charges, such that baryonic matter would enter a deconfinement state given some extreme conditions of temperature and pressure [1] . Later, evidence of the existence of QGP was obtained in 2000 at CERN; the following results in the same matter were published by physicists at the Brookhaven National Laboratory using the Relativistic Heavy-Ion Collider in 2004.

The importance of studying QGP comes from cosmological models in which the conditions of temperature and energy densities generated shortly after heavy-ion collisions match those of early stages after the Big Bang, at time intervals around 10^{-12}s. This way, at high collision energies, it was possible to reproduce what sometimes is called "mini big bang" events at the Large Hadron Collider, making QGP a great tool to probe the evolution right after "the birth of the universe".

Another essential feature of QGP is that it is a nearly ideal fluid with very low specific viscosity (ratio of shear viscosity to entropy density). The picture of energy densities or temperatures above the confinement energy scale leads to a state of matter in which hadronic matter can't exist. Instead, it is described by quarks and gluons strongly bound to their neighbors [1]. Heavy-ion collisions have helped us to overview the state of matter at high energies, precisely what is known as the QCD phase diagram, which essentially covers matter above a specific energy scale (dependent on temperature and baryon density/chemical potential) where hadronic (confined) matter cannot be present. A scheme of this phase diagram can be seen in Figure 1.

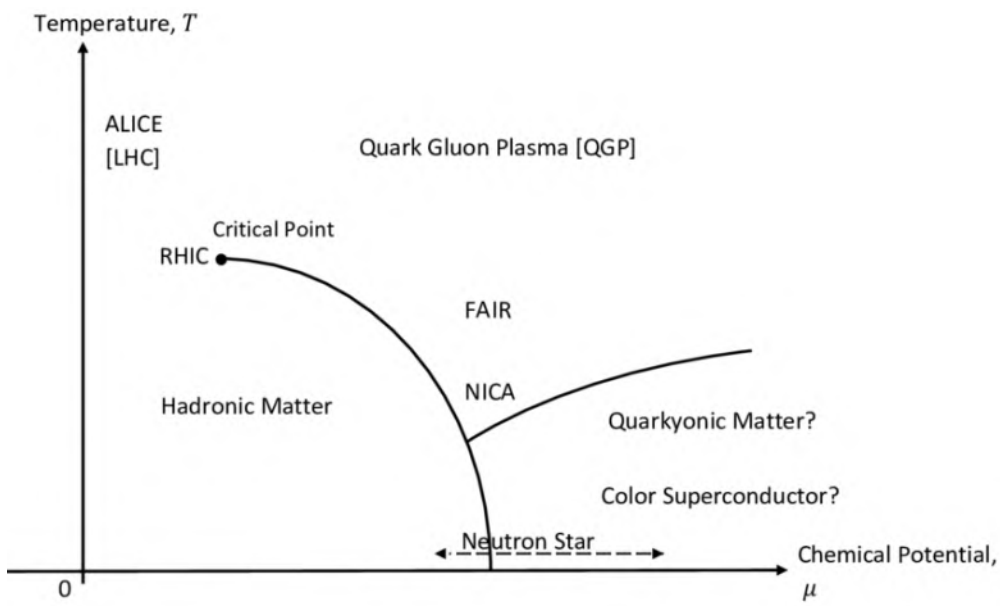

Figure 1: Phase diagram of QCD matter includes energy scale areas that some ion-collider facilities cover. Figure originally issued by Brett McInnes [2]

One crucial aspect in QCD is the concept of *asymptotic freedom*, although we won't develop the formalism behind this property, it is important to emphasize its significance in QGP formation. As QCD is the framework to describe the interactions between quarks and gluons, it is possible to quantitatively describe the strength of such interactions by a coupling constant α_s; the important part is that this constant may change its magnitude at different energy scales, specifically, low energy scales (long distances) imply a large interaction coefficient; whereas at high energy scales (short distances), the interaction coefficient becomes small. This feature describes weaker interactions between quarks and gluons as they come closer (rising energy density or temperature), allowing them to exist in a deconfined state, and creating the necessary conditions for QGP formation. Figure 2 depicts a graphical scheme of the running coupling as the energy scale (momentum transfer Q) rises.

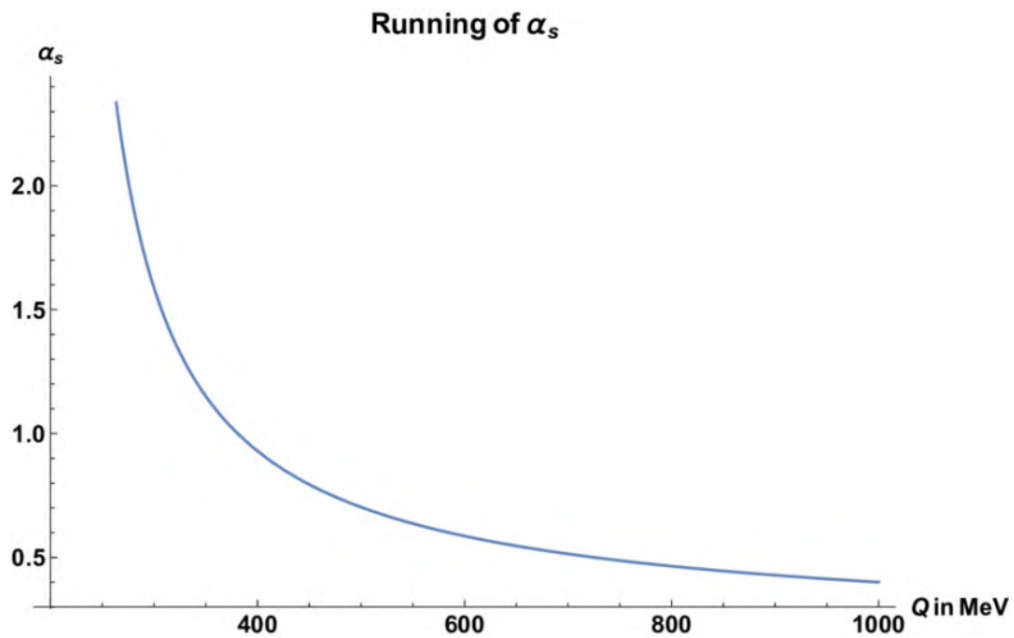

Figure 2: Asymptotic behavior of the QCD coupling constant as a function of momentum transfer Q. Image originally issued by Arman Margaryan [3].

The importance of asymptotic freedom for QGP description comes from empirical evidence that supports the existence of the latter and, therefore, also confirms the role of the theoretical predictions around strong interactions at high energies [4]. In 2004, for their contribution to the strong interaction theory, David J. Gross, David Politzer, and Frank Wilczek were awarded the Nobel Prize in physics, after experimental results at RHIC confirmed the existence of the new deconfined state of matter.

A helpful framework to work with is ideal relativistic hydrodynamics and some important aspects of QCD. Hydrodynamics makes it possible to simplify the complicated track of individual quarks and gluons in the system. Furthermore, the formulation of the relativistic Euler equations for fluid dynamics is quite simple, for conservation laws and equations of state relating to the system variables to use are the main components involved [5].

This project's principal hypothesis is whether heavy-ion collisions can be accurately simulated by stating initial conditions corresponding to an evolving continuous medium using relativistic hydrodynamics rather than a discrete system using quasi-particles or quantum molecular dynamics for the initial conditions. Taking advantage of the low viscosity properties of QGP, the feasibility of using ideal hydrodynamics will be tested. Finally, as the QGP evolves in a deconfined state such that there are virtually no inter-particle interactions between neighbors in the medium, we will test the accuracy of using the simple equation of state of an ideal gas.

The main goal of this project is to develop a code able to simulate the evolution of the early stages in heavy-ion collisions using relativistic hydrodynamics; the initial conditions of the incoming hadronic fluxes in these systems are intended to take similar properties as the colliding nuclei in heavy-ion experiments.

It is intended to correlate the experimental evidence of the thermodynamic conditions at which QGP forms, such as the temperature and energy density. [1] given certain initial energies, impact parameters, and nucleus types. Additionally, it is expected to qualitatively estimate the usefulness of ideal hydrodynamics simulations as a base model of heavy-ion collisions in early stages.

The first chapter in this text will focus on the formulation of the relativistic Euler equations of hydrodynamics in three dimensions and the numerical methods used to solve them, as well to review some macroscopic scenarios in which ideal hydrodynamics is well-established for its description.

In the second chapter, we will develop in more detail the relation between the thermodynamic variables the Euler equations work with an how they are related to the temperature by a equation of state, as well we will implement the initial conditions for a simplified scenario without nucleon interaction, and the energy density profile for the Monte Carlo Glauber model.

The third chapter we synthesize the results of 13 simulations with variations of the impact parameter, beam energy, nucleus type and initial condition's profile.

Finally, on the fourth chapter we will include the analyses of the results in chapter 3, and we will check the hypothesis formulated in this chapter, explore its implications in the state of the art, and make suggestions of tools and frameworks for possible improvements in this research.

2 Chapter I: Hydrodynamics

We are assuming that the medium moments after the collisions can be described via hydrodynamic equations, in particular, the relativistic Euler equations that describe the evolution of an inviscid fluid in terms of its density, pressure, velocity, and energy, all of them dependent on space-time coordinates x^μ. Depending on the scenario, the system of equations can go from $1+1$ D to $3+1$ D; these scenarios directly affect the velocity field components. The next step is their construction according to the conservation of mass and energy. Therefore, we will proceed to express them in their conservative form directly, that is, using new conservative variables to simplify the numerical techniques.

2.1 Relativistic Euler equations

The basis for describing QGP dynamics will be the CAFE code in its enhanced version in charge of Iván Álvarez from our group at IFM-UMSNH [6]. This set of programs deals with ideal Relativistic Hydrodynamic equations in $3+1$ dimensions and solves them over a fixed domain using numerical methods that will be described in this chapter. As stated before, the formulation of the relativistic Euler equations for fluid dynamics involves conservation laws and equations of state. test where implemented in 1+1, 2+1 and 3+1 dimensions with different configurations simulating various phenomena . To construct the aforementioned hydrodynamic equations, we will use the continuity equation of the stress-energy tensor $T^{\mu\nu}$ and the conservation of mass expressed in terms of the rest mass density ρ_0:

$$\frac{\partial}{\partial x^\mu}(\rho_0 u^\mu) = 0, \qquad\qquad \frac{\partial}{\partial x^\nu}(T^{\mu\nu}) = 0$$

where u^μ is the four-velocity of a fluid element, and the stress-energy tensor takes the form:

$$T^{\mu\nu} = \rho_0 h u^\mu u^\nu + p\eta^{\mu\nu} \tag{1}$$

In this case, $h = 1 + e + \frac{p}{\rho_0}$ is the specific enthalpy, e is the internal energy, and p the pressure of a fluid element; on the other hand, $\eta_{\mu\nu} = diag(-1, 1, 1, 1)$ are the components of the Minkowski metric at the space-time position of the fluid.

Following the conservation of rest mass and noting that $x^\mu = (x^0, x^1, x^2, x^3)$ where the 0 index indicates the temporal component such that $x^0 = t$, we can develop the first equation of the system taking into account that $u^0 = W$ is the Lorentz factor and v^i the components of the three-velocity:

$$\frac{\partial}{\partial t}(\rho_0 W) + \frac{\partial}{\partial x^i}(\rho_0 W v^i) = 0$$

and by defining a new variable $D = \rho_0 W$, we can get an equivalent expression

$$\frac{\partial}{\partial t}(D) + \frac{\partial}{\partial x^i}(D v^i) = 0 \tag{2}$$

Let's develop the next equations breaking up $T^{\mu\nu}$ by components, taking the spatial index $\mu = i$ and the temporal index $\mu = 0$ separately:

$$\frac{\partial}{\partial x^\nu}(T^{i\nu}) = \frac{\partial}{\partial t}(T^{i0}) + \frac{\partial}{\partial x^j}(T^{ij})$$

then, using equation (1) and the Kronecker delta δ^{ij}

$$\frac{\partial}{\partial t}(\rho_0 h W^2 v^i) + \frac{\partial}{\partial x^j}(\rho_0 h v^i v^j W^2 + p\delta^{ij}) = 0$$

defining a new variable $S^i = \rho_0 W^2 v^i$, we obtain a second conservation equation

$$\frac{\partial}{\partial t}(S^i) + \frac{\partial}{\partial x^j}(S^i v^j + p\delta^{ij}) = 0 \qquad (3)$$

For the last equation, we will take $\mu = 0$, add equation (2), and reduce the resulting equation defining the new variable $\tau = \rho_0 h W^2 - p - D$

$$\frac{\partial}{\partial x^\nu}(T^{0\nu}) = \frac{\partial}{\partial t}(T^{00}) + \frac{\partial}{\partial x^i}(T^{0i})$$

Looking at Equation (1), taking into account that $\eta_{00} = -1$ and $\eta_{0i} = 0$, and adding (2), we get

$$\frac{\partial}{\partial t}(\rho_0 h W^2 - p - D) + \frac{\partial}{\partial x^i}(\rho_0 h W^2 v^i - D v^i) = 0$$

Finally, taking τ and S^i the equation reduces to

$$\frac{\partial}{\partial t}(\tau) + \frac{\partial}{\partial x^i}(S^i - D v^i) = 0 \qquad (4)$$

Therefore, the set of equations (2), (3), and (4) conform to the relativistic Euler equations for the system to study, where D, S^i, and τ are the conservative variables. More specifically, these equations represent the conservation of rest mass density, the three-moment conservation, and the energy balance, respectively.

Finally, the initial value problem is expressed as follows:

$$
\begin{cases}
\frac{\partial}{\partial t}(D) + \frac{\partial}{\partial x^1}(Dv^1) + \frac{\partial}{\partial x^2}(Dv^2) + \frac{\partial}{\partial x^3}(Dv^3) = 0 \\
\frac{\partial}{\partial t}(S^1) + \frac{\partial}{\partial x^1}(S^1v^1 + p) + \frac{\partial}{\partial x^2}(S^1v^2) + \frac{\partial}{\partial x^3}(S^1v^3) = 0 \\
\frac{\partial}{\partial t}(S^2) + \frac{\partial}{\partial x^1}(S^2v^1) + \frac{\partial}{\partial x^2}(S^2v^2 + p) + \frac{\partial}{\partial x^3}(S^2v^3) = 0 \\
\frac{\partial}{\partial t}(S^3) + \frac{\partial}{\partial x^1}(S^3v^1) + \frac{\partial}{\partial x^2}(S^3v^2) + \frac{\partial}{\partial x^3}(S^3v^3 + p) = 0 \\
\frac{\partial}{\partial t}(\tau) + \frac{\partial}{\partial x^1}(S^1 - Dv^1) + \frac{\partial}{\partial x^2}(S^2 - Dv^2) + \frac{\partial}{\partial x^3}(S^3 - Dv^3) = 0 \\
\text{With the following initial conditions in the primitive variables:} \\
v^1(0, x^1, x^2, x^3),\ v^2(0, x^1, x^2, x^3),\ v^3(0, x^1, x^2, x^3)\ ... \\
\rho_0(0, x^1, x^2, x^3),\ p(0, x^1, x^2, x^3),\ e(0, x^1, x^2, x^3)
\end{cases}
\tag{5}
$$

2.2 Finite volume method

We will use the finite volume method to solve the previous system of equations; this numerical technique allows us to write the PDEs in their conservative form, performing a flux balance through a control volume, making it a suitable method for hydrodynamics involving conservation laws. The FVM also assumes that the distribution of a general quantity $\mathbf{u}_i$ expresses a discontinuity at the interface between neighboring cells, thus manifesting a sequence of local Riemann problems to be solved. In this text, we will use only the HLLE Riemann Solver (section 2.3) to perform the time integration because it's simple and only requires the eigenvalues of the Jacobian matrix of the flux formula.

To describe the FVM step by step, we will illustrate it in 1+1 dimensions, and later on, we will take a generalized formulation for the 3+1 dimension case. The main idea is to perform a discretization of the PDEs and integrate them over a control volume (see figure 3) to obtain algebraic equations in terms of the fluxes.

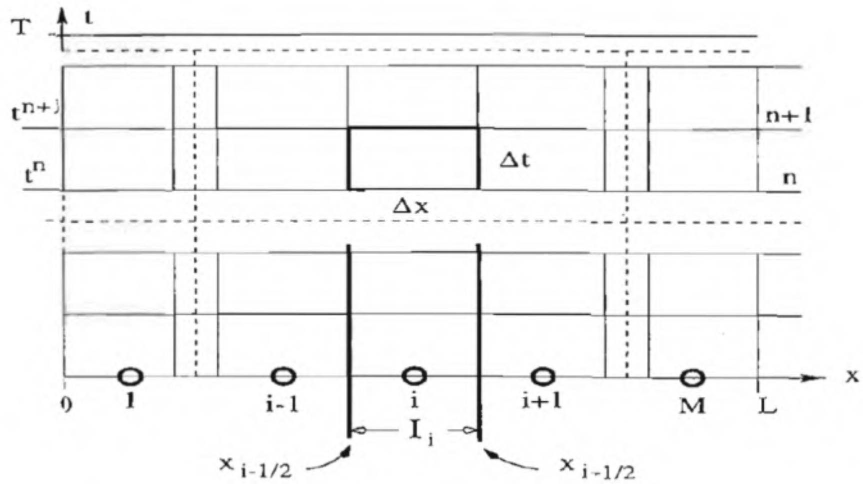

Figure 3: Control volume $V = [x_{i-1/2}, x_{1+1/2}] \times [t^n, t^{n+1}]$ (Luciano Rezolla, 2018)

In 1+1 dimensions, the conservative form of the Euler equations is expressed as:

$$\frac{\partial \mathbf{u}}{\partial t} + \frac{\partial \mathbf{F}(\mathbf{u})}{\partial x} = 0 \tag{6}$$

where **u** is the vector conformed by the variables D, S and τ, whereas **F** is the flux vector in the x-direction. These vectors take the following form:

$$\mathbf{u} = \begin{pmatrix} D \\ S \\ \tau \end{pmatrix}, \qquad \mathbf{F}^1 = \begin{pmatrix} Dv \\ Sv + p \\ S - Dv \end{pmatrix},$$

The integral form of equation 6 can be written by first performing a space integration, such that:

$$\frac{d}{dt}\int_{x_{i-1/2}}^{x_{i+1/2}} \mathbf{u}(x,t)dx + \mathbf{F}(\mathbf{u}(x_{i+1/2},t)) - \mathbf{F}(\mathbf{u}(x_{i-1/2},t)) = 0$$

following by a time integration from t^n to t^{n+1}

$$\int_{x_{i-1/2}}^{x_{1+1/2}} \mathbf{u}(x,t^{n+1})dx - \int_{x_{i-1/2}}^{x_{1+1/2}} \mathbf{u}(x,t^{n})dx =$$
$$-\left(\int_{t^n}^{t^{n+1}} \mathbf{F}(\mathbf{u}(x_{i+1/2},t))dt - \int_{t^n}^{t^{n+1}} \mathbf{F}(\mathbf{u}(x_{i-1/2},t))dt\right).$$

Now, we can re-write the integral forms of these equations by defining the two new quantities

$$\overline{\mathbf{u}}_i^n = \frac{1}{\Delta x}\int_{x_{i-1/2}}^{x_{1+1/2}} \mathbf{u}(x,t^n)dx$$

and

$$\overline{\mathbf{F}}_{i\pm1/2} = \frac{1}{\Delta t}\int_{t^n}^{t^{n+1}} \mathbf{F}(\mathbf{u}(x_{i\pm1/2},t))dt$$

finally obtaining the semi-discrete form of equation 6:

$$\frac{\overline{\mathbf{u}}_i^{n+1} - \overline{\mathbf{u}}_i^n}{\Delta t} = \frac{\partial\overline{\mathbf{u}}}{\partial t} = -\frac{\overline{\mathbf{F}}_{i+1/2} - \overline{\mathbf{F}}_{i-/2}}{\Delta x} \tag{7}$$

In terms of the primitive variables (ρ_0, p, v^i and e), this system happens to be undetermined; six variables related by five equations.

Thermodynamical properties have to be stated to solve the previous equations; we must use an equation of state correlating three variables, being the ideal gas the simplest one:

$$p = \rho_0 e(\gamma - 1)$$

where $\gamma = C_p/C_v$ is the ratio between constant pressure and constant volume heat capacities. Since the ideal gas equation relates the pressure with the other primitive variables, we can close the previous system of PDEs:

$$p = \rho_0(\gamma - 1)\left[\frac{\tau D(1-W) + p(q - W^2)}{DW}\right]$$

Furthermore, taking W in terms of τ, p, D, and S^i, this transcendental equation can be approximately solved using the Newton-Raphson method of finding roots.

We can rewrite equation (6) applying the chain rule as follows:

$$\frac{\partial \mathbf{u}}{\partial t} + \frac{\partial \mathbf{F}}{\partial \mathbf{u}}\frac{\partial \mathbf{u}}{\partial x} = 0 \tag{8}$$

From this equation, the terms $\frac{\partial \mathbf{F}}{\partial \mathbf{u}}$ correspond to the Jacobian Matrix of the flux vector. The next step is to obtain the step their three eigenvalues [7]:

$$\lambda_1 = v, \qquad \lambda_2 = \frac{v + c_s}{1 + vc_s}, \qquad \lambda_3 = \frac{v - c_s}{1 - v^1 c_s}$$

where the constant $c_s = \sqrt{\frac{\partial P}{\partial \rho_0}/\rho_0}$ is the speed of sound. To implement it, we will have to express c_s in terms of the primitive variables p and ρ_0; to do so, we must rewrite the specific enthalpy as $h = 1 + \frac{p}{\rho_0}\frac{\gamma}{\gamma-1}$ and take the following relation:

$$\begin{aligned} hc_s^2 &= \frac{\partial P}{\partial \rho_0} + \left(\frac{p}{\rho_0^2}\right)\frac{\partial P}{\partial e} \\ \hookrightarrow &\quad \frac{p(\gamma-1)\gamma}{\rho_0(\gamma-1) + p\gamma}. \end{aligned} \tag{9}$$

Moreover, taking a look at equation 8, we can interpret that, physically, the eigenvalues of **F** represent the speeds of a wave-like propagation.

It's worth noting that equation 7 assumes the knowledge of the averaged flux vector $\overline{\mathbf{F}}$. To follow through this scheme, it is necessary to make approximations and assumptions over $\overline{\mathbf{F}}$ to perform a time evolution. In the following section, we will explore a method to obtain the fluxes given the direction of propagation of information over the control volume.

2.3 HLLE approximate-flux Riemann solver

In the context of hydrodynamics, the Riemann solver developed in 1983 by Harten, Lax, and van-Leer and five years later enhanced by Einfeldt (HLLE) is widely used for its simplicity and balance between computational efficiency and accuracy. The core idea of this solver is that two waves propagate in opposite directions with velocities λ_R and λ_L, respectively, after the decay of the initial discontinuity and generating one state $\mathbf{u}^{HLLE}$ in between:

$$\mathbf{u} = \begin{cases} \mathbf{u}_L & \text{if } \quad x/t < \lambda_L \\ \mathbf{u}^{HLLE} & \text{if } \lambda_L < x/t < \lambda_R \\ \mathbf{u}_R & \text{if } \quad x/t > \lambda_R \end{cases} \tag{10}$$

where λ_L and λ_R are the largest speeds moving to the left and moving to the right respectively.

To obtain an expression for $\mathbf{u}^{HLLE}$ we must perform an integration of equation 6 over the control volume shown in figure 4. The integration over the time interval $[0, T]$ is:

$$\mathbf{u}(x, T) = \mathbf{u}(x, 0) - \int_0^T \frac{\partial \mathbf{F}(\mathbf{u}(t, x))}{\partial x} dt$$

Now integrating over the space interval $[-\Gamma, \Gamma]$, the equation becomes

$$\int_{-\Gamma}^{\Gamma} \mathbf{u}(x, T) dx = \int_{-\Gamma}^{\Gamma} \mathbf{u}(x, 0) dx + \int_0^T \mathbf{F}(\mathbf{u}(-\Gamma, t)) dt - \int_0^T \mathbf{F}(\mathbf{u}(\Gamma, t)) dt. \tag{11}$$

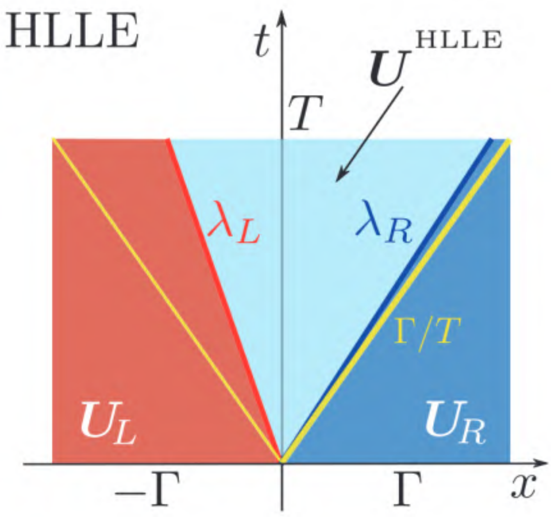

Figure 4: Control volume diagram to approximate the HLLE flux, figure taken from [7]

We can express the right-hand side in terms of $\mathbf{u}_L$ and $\mathbf{u}_R$ using equation 10 and split the first term:

$$\int_{-\Gamma}^{\Gamma} \mathbf{u}(x,T)dx = \int_{-\Gamma}^{0} \mathbf{u}_L dx + \int_{0}^{\Gamma} \mathbf{u}_R dx \int_{0}^{T} \mathbf{F}(\mathbf{u}_L)dt - \int_{0}^{T} \mathbf{F}(\mathbf{u}_R)dt$$

Taking $\mathbf{F}(\mathbf{u}_R) = \mathbf{F}_R$, $\mathbf{F}(\mathbf{u}_L) = \mathbf{F}_L$ and evaluating, we obtain

$$\int_{-\Gamma}^{\Gamma} \mathbf{u}(x,T)dx = \Gamma(\mathbf{u}_R + \mathbf{u}_L) + T(\mathbf{F}_L - \mathbf{F}_R) \tag{12}$$

Now, given the conditions in 10 we can split the left-hand side of equation 11 to obtain:

$$\begin{aligned}\int_{-\Gamma}^{\Gamma} \mathbf{u}(x,T)dx &= \int_{-\Gamma}^{T\lambda_L} \mathbf{u}_L dx + \int_{T\lambda_L}^{T\lambda_R} \mathbf{u}_{HLLE} dx + \int_{T\lambda_R}^{\Gamma} \mathbf{u}_R dx \\ &= \mathbf{u}_L(T\lambda_L + \Gamma) + \mathbf{u}_{HLLE}(\lambda_R - \lambda_L)T + \mathbf{u}_R(\Gamma - T\lambda_R)\end{aligned} \tag{13}$$

Comparing the righ-hand sides of equations 12 and 13 we find

$$\mathbf{u}_{HLLE} = \frac{\lambda_R \mathbf{u}_R - \lambda_L \mathbf{u}_L + \mathbf{F}_L - \mathbf{F}_R}{\lambda_R - \lambda_L} \tag{14}$$

Now we have to obtain the numerical flux $\mathbf{F}_{HLLE}$, to do so, we have to integrate equation 6 either in the volume $[-\Gamma, 0] \times [0, T]$ or $[0, \Gamma] \times [0, T]$ as shown in figure 4. Following the latter:

$$\int_0^\Gamma \mathbf{u}(x,T)dx - \int_0^\Gamma \mathbf{u}(x,0)dx + T(\mathbf{F}_R - \mathbf{F}_{HLLE}) = 0$$
$$\hookrightarrow \quad \Gamma(\mathbf{u}_{HLLE} - \mathbf{u}_R) + T(\mathbf{F}_R - \mathbf{F}_{HLLE}) = 0$$

Solving for $\mathbf{F}_{HLLE}$ and noting that $\Gamma = T\lambda_R$, we get

$$\mathbf{F}_{HLLE} = \lambda_R \mathbf{u}_{HLLE} - \lambda_R \mathbf{u}_R + \mathbf{F}_R \tag{15}$$

Finally, plugging equation 14 into equation 15 gives

$$\mathbf{F}^{HLLE} = \frac{\lambda_R \mathbf{F}_L - \lambda_L \mathbf{F}_R + \lambda_R \lambda_L (\mathbf{u}_R - \mathbf{u}_L)}{\lambda_R - \lambda_L} \tag{16}$$

Where λ_R and λ_L are defined by:

$$\begin{cases} \lambda_R = \max(0,\ \lambda_1^R,\ \lambda_2^R,\ \lambda_3^R,\ \lambda_1^L,\ \lambda_2^L,\ \lambda_3^L) \\ \lambda_L = \min(0,\ \lambda_1^R,\ \lambda_2^R,\ \lambda_3^R,\ \lambda_1^L,\ \lambda_2^L,\ \lambda_3^L) \end{cases}$$

Where $\lambda_i^{L,R}$ are the eigenvalues of the Jacobian matrix of the left-hand side of equation 8 evaluated at the left and right boundaries of the intercell.

An analogous approach can be done for the $3+1$ dimensional case taking advantage of the linear nature of equation 6 we can add the two flux vectors along y and z directions, generalizing the former differential equation:

$$\frac{\partial \mathbf{u}}{\partial t} + \frac{\partial \mathbf{F}^1(\mathbf{u})}{\partial x^1} + \frac{\partial \mathbf{F}^2(\mathbf{u})}{\partial x^2} + \frac{\partial \mathbf{F}^3(\mathbf{u})}{\partial x^3} = 0 \tag{17}$$

The semi-discrete form of this system is then expressed as:

$$\frac{\partial \overline{\mathbf{u}}}{\partial t} = -\frac{\overline{\mathbf{F}}^1_{i+1/2} - \overline{\mathbf{F}}^1_{i-/2}}{\Delta x^1} - \frac{\overline{\mathbf{F}}^2_{i+1/2} - \overline{\mathbf{F}}^2_{i-/2}}{\Delta x^2} - \frac{\overline{\mathbf{F}}^3_{i+1/2} - \overline{\mathbf{F}}^3_{i-/2}}{\Delta x^3} \tag{18}$$

As in the $1+1$ dimensional case, equation 18 assumes the knowledge of the averaged flux vectors $\overline{\mathbf{F}}^1$, $\overline{\mathbf{F}}^2$ and $\overline{\mathbf{F}}^3$, to construct these, we will rely again on the chain rule to rewrite equation 17 as:

$$\frac{\partial \mathbf{u}}{\partial t} + \frac{\partial \mathbf{F}^1}{\partial \mathbf{u}}\frac{\partial \mathbf{u}}{\partial x^1} + \frac{\partial \mathbf{F}^2}{\partial \mathbf{u}}\frac{\partial \mathbf{u}}{\partial x^2} + \frac{\partial \mathbf{F}^3}{\partial \mathbf{u}}\frac{\partial \mathbf{u}}{\partial x^3} = 0 \tag{19}$$

This time, we will obtain five eigenvalues for each Jacobian matrix [7]:

$$\begin{cases} \frac{\partial \mathbf{F}^1}{\partial \mathbf{u}}: & \lambda_1 = v^1, \quad \lambda_2 = v^1, \quad \lambda_3 = v^1, \quad \lambda_4 = \frac{v^1+c_s}{1+v^1c_s}, \quad \lambda_5 = \frac{v^1-c_s}{1-v^1c_s} \\ \frac{\partial \mathbf{F}^2}{\partial \mathbf{u}}: & \lambda_1 = v^2, \quad \lambda_2 = v^2, \quad \lambda_3 = v^2, \quad \lambda_4 = \frac{v^2+c_s}{1+v^2c_s}, \quad \lambda_5 = \frac{v^2-c_s}{1-v^2c_s} \\ \frac{\partial \mathbf{F}^3}{\partial \mathbf{u}}: & \lambda_1 = v^3, \quad \lambda_2 = v^3, \quad \lambda_3 = v^3, \quad \lambda_4 = \frac{v^3+c_s}{1+v^3c_s}, \quad \lambda_5 = \frac{v^3-c_s}{1-v^3c_s} \end{cases} \tag{20}$$

If we follow the same steps for the $1+1$ dimensional case, for the flux vectors in each direction separately, we end up obtaining the following expressions

$$\begin{cases} \mathbf{F}^1_{HLLE} = \frac{\lambda_R \mathbf{F}^1_L - \lambda_L \mathbf{F}^1_R + \lambda_R\lambda_L(\mathbf{u}_R - \mathbf{u}_L)}{\lambda_R - \lambda_L} \\ \mathbf{F}^2_{HLLE} = \frac{\lambda_R \mathbf{F}^2_L - \lambda_L \mathbf{F}^2_R + \lambda_R\lambda_L(\mathbf{u}_R - \mathbf{u}_L)}{\lambda_R - \lambda_L} \\ \mathbf{F}^3_{HLLE} = \frac{\lambda_R \mathbf{F}^3_L - \lambda_L \mathbf{F}^3_R + \lambda_R\lambda_L(\mathbf{u}_R - \mathbf{u}_L)}{\lambda_R - \lambda_L} \end{cases} \tag{21}$$

Where λ_R and λ_R are given by the eigenvalues of the Jacobian matrices in each direction given in equation 20 as:

$$\begin{cases} \lambda_R = \max(0,\ \lambda_1^R,\ \lambda_2^R,\ \lambda_3^R,\ \lambda_4^R,\ \lambda_5^R,\ \lambda_1^L,\ \lambda_2^L,\ \lambda_3^L,\ \lambda_4^L,\ \lambda_5^L) \\ \lambda_L = \min(0,\ \lambda_1^R,\ \lambda_2^R,\ \lambda_3^R,\ \lambda_4^R,\ \lambda_5^R,\ \lambda_1^L,\ \lambda_2^L,\ \lambda_3^L,\ \lambda_4^L,\ \lambda_5^L) \end{cases}$$

It's important to note that fluxes $\mathbf{F}^i_{R,L}$ in the right-hand side of equations 21 are obtained in terms of the conservative variables, unlike the eigenvalues in 21 which are written in terms of the primitive variables; moreover, the discrete nature of the finite volume method, which assumes a piece-wise constant behavior of $\mathbf{u}$ as shown in equation 7, loses any information of the variables in the cell interfaces. To address this problem we will improve the solutions by using the *minmod* reconstruction technique. The minmod reconstructor assumes a linear behavior of the solutions within cells, defined in each direction as follows:

$$
\begin{aligned}
\text{for } x^1: \qquad & \mathbf{u}^R_{i,j,k} = \mathbf{u}_{i+1/2,j,k} + \sigma_{i+1/2}(x^1_i - x^1_{i+1/2}) \\
& \mathbf{u}^L_{i,j,k} = \mathbf{u}_{i-1/2,j,k} + \sigma_{i-1/2}(x^1_i - x^1_{i-1/2}) \\
\text{for } x^2: \qquad & \mathbf{u}^R_{i,j,k} = \mathbf{u}_{i,j+1/2,k} + \sigma_{j+1/2}(x^2_j - x^2_{j+1/2}) \\
& \mathbf{u}^L_{i,j,k} = \mathbf{u}_{i,j-1/2,k} + \sigma_{j-1/2}(x^2_j - x^2_{j-1/2}) \\
\text{for } x^3: \qquad & \mathbf{u}^R_{i,j,k} = \mathbf{u}_{i,j,k+1/2} + \sigma_{k+1/2}(x^3_k - x^3_{k+1/2}) \\
& \mathbf{u}^L_{i,j,k} = \mathbf{u}_{i,j,k-1/2} + \sigma_{k-1/2}(x^3_k - x^3_{k-1/2})
\end{aligned}
\tag{22}
$$

where σ is also defined for each direction by:

$$
\begin{aligned}
\text{for } x^1: \qquad & \sigma_i = \text{minmod}\left(\frac{\mathbf{u}_{i,j,k} - \mathbf{u}_{i-1,j,k}}{x^1_i - x^1_{i-1}}, \frac{\mathbf{u}_{i+1,j,k} - \mathbf{u}_{i,j,k}}{x^1_{i+1} - x^1_i}\right) \\
\text{for } x^2: \qquad & \sigma_i = \text{minmod}\left(\frac{\mathbf{u}_{i,j,k} - \mathbf{u}_{i,j-1,k}}{x^2_j - x^2_{j-1}}, \frac{\mathbf{u}_{i,j+1,k} - \mathbf{u}_{i,j,k}}{x^2_{j+1} - x^2_j}\right) \\
\text{for } x^3: \qquad & \sigma_i = \text{minmod}\left(\frac{\mathbf{u}_{i,j,k} - \mathbf{u}_{i,j,k-1}}{x^3_k - x^3_{k-1}}, \frac{\mathbf{u}_{i,j,k+1} - \mathbf{u}_{i,j,k}}{x^3_{k+1} - x^3_k}\right)
\end{aligned}
\tag{23}
$$

the minmod function which defines the slope inside the cell is:

$$
\text{minmod}(\alpha,\beta)
\begin{cases}
\alpha & \text{if} \quad |\alpha| < |\beta| \text{ and } \alpha\beta > 0 \\
\beta & \text{if} \quad |\beta| < |\alpha| \text{ and } \alpha\beta > 0 \\
0 & \text{if} \quad \alpha\beta \leq 0
\end{cases}
\tag{24}
$$

Using the set of equations in 20 it is now possible to perform an integration over time using the Runge-Kutta method of order 3, addressing the discontinuities in equation 17. Finally, after the time step evolution, we need to recover the primitive variables in terms of the conservative ones as:

$$v^i = \frac{S^i}{\tau + p + D}$$

$$\rho_0 = D\sqrt{1 - v^2}$$

remembering that the pressure p was written in terms of D, τ and W to be obtained by the Newton-Raphson method.

2.4 Characteristic simulations

Three main simulations were tested to check the viability of the code, one was made with a 1D head-on stream configuration; in a 2D domain, the relativistic Riemann problem and the relativistic Emery wind tunnel system; finally, in a 3D domain, we include the relativistic Kelvin Helmholtz instability.

The *head-on stream* configuration is probably the simplest approximation to head-on interactions, as two main streams at high velocities in opposite directions, come into contact at the center of the domain, creating a shock that propagates in both directions. The shock generates a sudden deceleration of the medium.

Given a domain of $-1 \leq x \leq 1$ this configuration has the following conditions:

$$(\rho_0,\ p,\ v^x) = \begin{cases} (1.0,\ 0.001,\ -0.99) & \text{if} \quad x > 0 \\ (1.0,\ 0.001,\ 0.99) & \text{if} \quad x < 0 \end{cases}$$

In heavy-ion collision experiments, an essential consequence of head-on nuclear interactions is the hydrodynamic expansion of the media, this simulation can give us a rough idea of what to expect in more complex configurations.

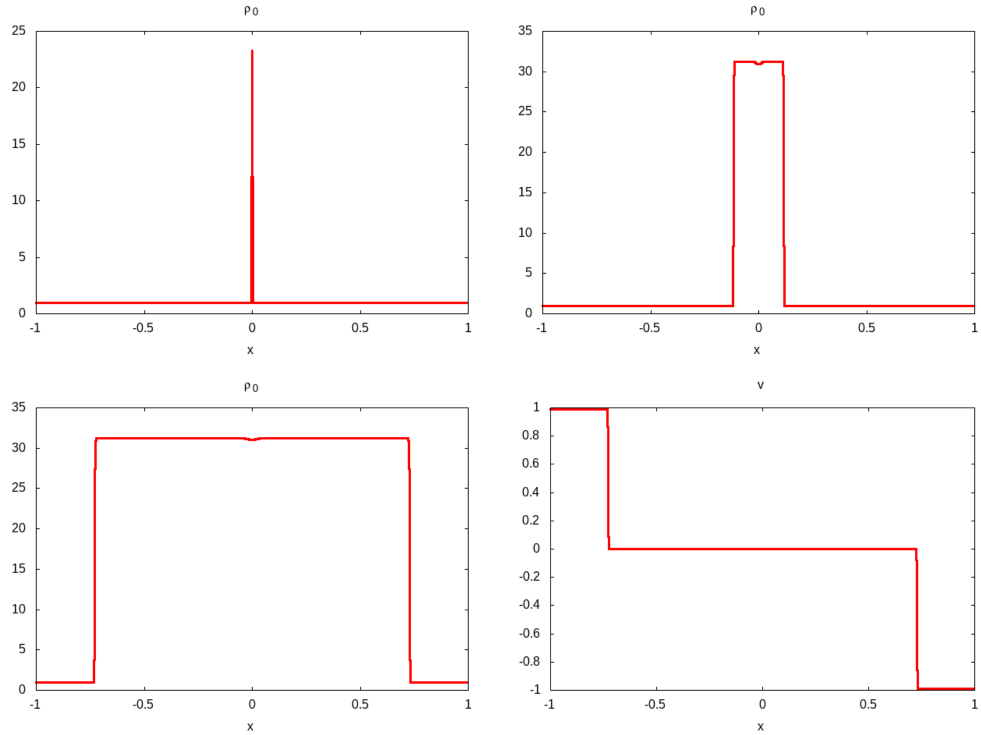

Figure 5: Rest mass density and velocity distributions in a $[-1, 1]$ domain. We show snapshots at different evolution times: at $t = 0.005$ (top left) where we observe a peak given a sudden increase of the rest mass density; at $t = 0.4$ (top right), showing a medium expansion over the domain; and $t = 2.5$ (bottom left) where the medium almost covers all the domain. The velocity distribution (bottom right) shows a sudden decrease in the velocity in the center, the domain covering the expansion in the latter figure corresponds to the deceleration range.

Next, we include the *relativistic 2D Riemann problem* which involves different initial conditions in four quadrants inside the domain $[-1.0, 1.0] \times [-1.0, 1.0]$. The initial states are defined by the following configuration:

$$
(\rho,\ p,\ v^x,\ v^y) = \begin{cases} (0.1,\ 1.0,\ 0.99,\ 0) & \text{if} \quad x < 0 \ \text{ and } \ y > 0 \\ (0.1,\ 0.01,\ 0,\ 0) & \text{if} \quad x > 0 \ \text{ and } \ y > 0 \\ (0.5,\ 1.0,\ 0,\ 0) & \text{if} \quad x < 0 \ \text{ and } \ y < 0 \\ (0.1,\ 1.0,\ 0,\ 0.99) & \text{if} \quad x > 0 \ \text{ and } \ y < 0 \end{cases}
$$

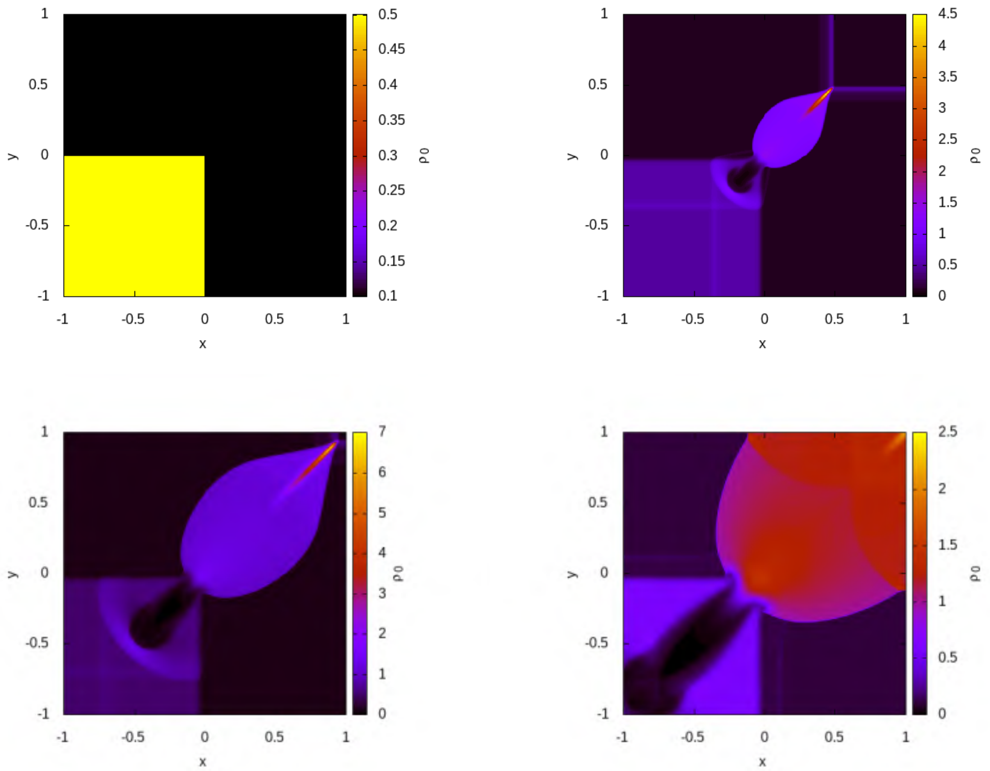

Figure 6: Relativistic 2D Riemann problem at different evolution times. The snapshots correspond to the rest mass density at $t = 0$ (top left), $t = 0.45$ (top right), $t = 0.91$ (bottom left) and $t = 1.83$ (bottom right).

In figure 6 we can observe four snapshots of the evolution of the system, specifically the evolution of rest mass density over time. It is worth noting that the nature of the initial conditions made it possible to reproduce characteristic phenomena in fluid dynamics such as a bow shock in the fourth quadrant and a jet flowing in the opposite direction.

To test the implementation of specific boundary conditions, we include the configuration of the *Emery wind tunnel* problem in the domain $-1.5 \leq z \leq 1.5$ and $-0.5 \leq y \leq 0.5$. It has an incoming flow in the z-direction with $p = 1.0$, $\rho_0 = 1.4$, $v^z = 0.99$ and $v^y = 0$, and a reflecting step starting at one-fifth from the vertical and horizontal axes.

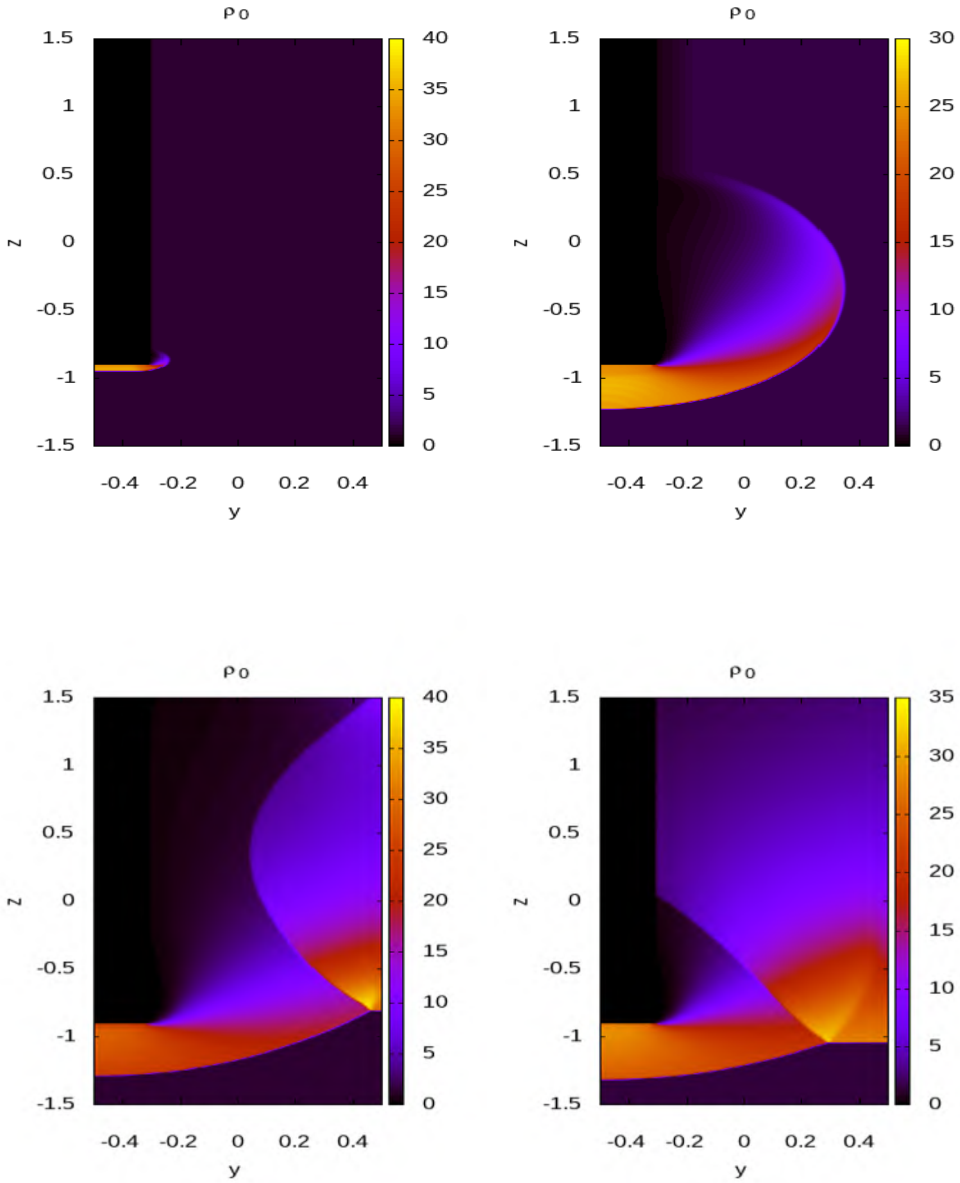

Figure 7: Rest mass density evolution in the relativistic Emery wind tunnel in a domain defined by $[-0.5,\ 0.5] \times [-1.5,\ 1.5]$. The snapshots correspond to times $t = 0.1$ (top left), $t = 1.4$ (top right), $t = 2.8$ (bottom left) and $t = 4.2$ (bottom right)

The snapshots above show the system's evolution from $t = 0.1$ to $t = 4.2$ (from top left to bottom right). From this simulation, it is possible to note that the code deals with standard flow discontinuities; it can be seen how the flow reflects away from the step at $t = 0.1$, expands, and generates a bow shock with the incoming stream at $t = 1.4$, bounces to the left in the right boundary at $t = 2.8$ and bounces back to the right in $t = 4.2$.

For the 3D test, we show the relativistic Kelvin Helmholtz instability. This phenomenon occurs when there is a perturbation in the initial conditions across the interface between two fluids. This test, in particular, shows a $[-0.5,\ 0.5] \times [-1,\ 1]$ domain filled with gas, and a strip in the middle with a different state gas. The configuration for reads:

$$\rho(y) = \begin{cases} \rho_0 + \rho_1 \tanh[(z - 0.5)/a], & \text{if} \quad z > 0 \\ \rho_0 - \rho_1 \tanh[(z + 0.5)/a], & \text{if} \quad z \leq 0 \end{cases}$$

$$v^y(z) = \begin{cases} V_s \tanh[(z - 0.5)/a], & \text{if} \quad z > 0 \\ V_s \tanh[(z + 0.5)/a], & \text{if} \quad z \leq 0 \end{cases}$$

$$v^z(y,z) = \begin{cases} A_0 V_s \sin(2\pi y) \exp[-(z - 0.5)^2/\sigma], & \text{if} \quad z > 0 \\ -A_0 V_s \sin(2\pi y) \exp[-(z + 0.5)/\sigma], & \text{if} \quad z \leq 0 \end{cases}$$

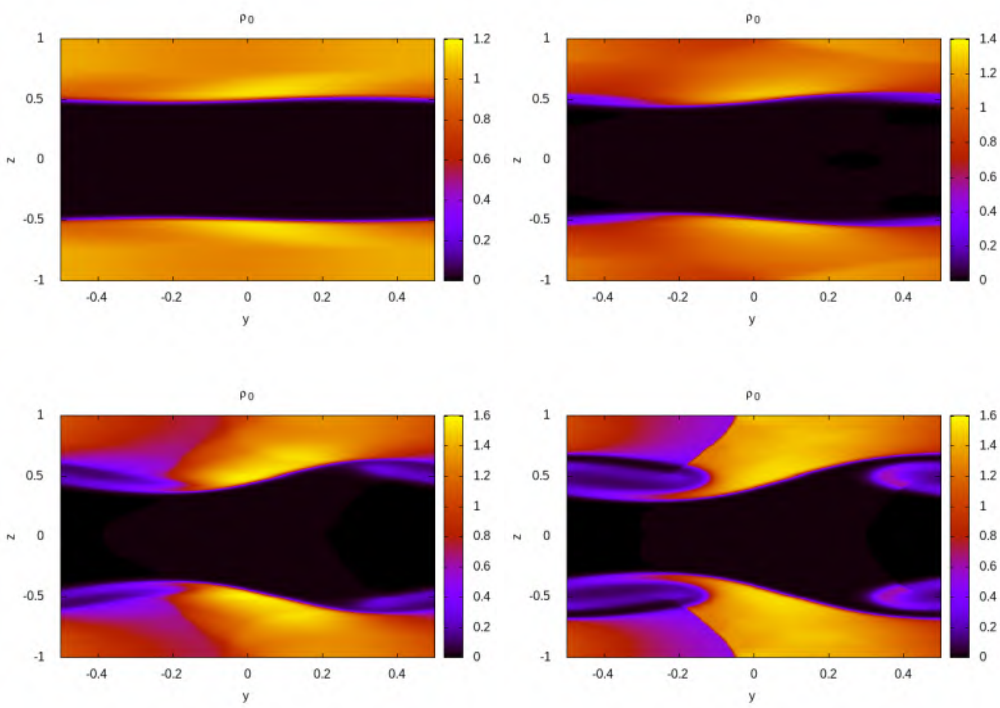

Figure 8: Rest mass density evolution in the relativistic 3D Kelvin Helmholtz in a domain defined by $[-0.5,\ 0.5] \times [-1,\ 1]$. The snapshots correspond to times $t = 0.5$ (top left), $t = 1.5$ (top right), $t = 2.5$ (bottom left) and $t = 3.5$ (bottom right)

Where $\rho_0 = 0.505$, $\rho_1 = 0.495$, $a = 0.01$, $A_0 = 0.1$, $V_s = 0.5$ and $\sigma = 0.1$. A third component for v^x is given by a random number between 0 and 0.01, which gives the 3D nature of the problem to a small extent. The figure 8 above shows the system evolution from $t = 0.5$ to $t = 3.5$ in four snapshots. It is important to note here that the minmod reconstructor fails to capture the development of small structures in the system in comparison to other high-order schemes [6].

So far, the code works to a limited extent, specifically, reproducing some macroscopic phenomena. The following chapter will introduce a different approach in configurations as well as add a microscopic scale to recreate an accurate configuration for heavy-ion collisions, both geometrically and at the thermodynamic level; including impact parameters (the collision intersection) from $r = 0$ to all the transverse extension of the incoming the beams in the former, and including the temperature for the equation of state in the latter.

3 Chapter II: Implementation

The equations that CAFE solves have great applicability in astrophysics research since hydrodynamics, primarily a macroscopic framework, converges with fluid descriptions at large scales. Instead of explicitly describing particle interactions, we describe the evolution of continuous properties such as velocity, pressure, and density. For this reason, the code must be adapted to cover microscopic scenarios, and reproduce the thermodynamic values that heavy-ion collision experiments estimate.

It is imperative to re-scale the units to make measurements. To do so, the velocity units are set to $v = c = 1$, where c is the speed of light in vacuum, note that this setting makes time and space have the same units. In this case, we will work with length in units of 1 fm $= 10^{-15}$m and time in units of fm$/c$ to avoid ambiguity. With these units in mind, it is possible to re-scale the pressure and rest mass density. In microscopic scenarios where relativistic dynamics is involved, energy and mass have the same units as well so that 1 GeV $= 1.8 \times 10^{-27}$ kg. Using natural units where $\hbar = 1$ and including equations of state in terms of the temperature, it is possible to obtain values for T, usually in terms of MeV or GeV.

For the case of an ultra-relativistic ideal gas, the adiabatic index is $\gamma = 4/3$ [8], therefore, the ideal gas equation becomes:

$$p = \frac{\epsilon}{3} = \frac{\rho_0}{3}(1 + e) \tag{25}$$

where ϵ represents the energy density, which is expressed with its internal energy and rest mass contributions.

One important factor to study is the evolution of the temperature T since its values give us a close understanding of the QGP evolution. Since the QCD scale is in the order of $\Lambda_{QCD} \sim 200\,\text{MeV} - 300\,\text{MeV}$, it is expected that temperatures around that scale would lead us to a deconfined state of matter [9] [10] . It is possible to calculate the temperature from the energy density of a non-interacting gas consisting of quarks and gluons, this is obtained according to the occupation number given by the distributions:

$$n = \frac{g}{e^{\frac{E}{T}} \pm 1}$$

where the $+$ sign is used for quarks and the $-$ sign for gluons. In this way, the energy density is just the integral over energy levels from 0 to ∞ of E times n. Therefore, the energy density results:

$$\epsilon_{QGP} = \left(g_g + \frac{7}{8}(g_q + g_{\bar{q}}) \right) \frac{\pi^2}{30} T^4$$

where the degenerate states are $g_g = 16$ for gluons and $g_q + g_{\bar{q}} = 24$ for quarks. With these aspects in mind, the equation of an ideal gas in terms of the temperature for a QGP finally becomes:

$$p = 37 \frac{\pi^2}{90} T^4 \tag{26}$$

The next step is to use appropriate initial conditions to describe the hydrodynamical evolution using the relativistic Euler equations described in Chapter 1.

3.1 Initial conditions for a simplified scenario

The first attempt to simulate the QGP dynamics neglected sub-atomic interactions between nucleons, relying purely on a confined ideal gas with the mass density following the Wood-Saxon distribution over the radius of a cylinder [11] :

$$\rho(r) = \rho_0 \frac{1}{1 + \exp[\frac{r - r_N}{\delta}]} \tag{27}$$

The initial conditions for ρ_0, p and v_z are the following:

$$(\rho_0,\ p,\ v^z) = \begin{cases} (\rho(r_{max}),\ \rho(r_{max})/3,\ 0) & \text{if} \quad r > r_N \\ (\rho(r),\ \rho(r)/3,\ v) & \text{if} \quad r < r_N \end{cases}$$

where r_N is the nuclear radius and r_{max} corresponds to the boundaries of the domain where the distribution $\rho(r)$ reaches a minimum, that is, at $x = \pm 15$ fm and $y = \pm 15$ fm. On the other hand, the conditions for v are:

$$v = \begin{cases} 0.99c & \text{if} \quad \sqrt{(x-b)^2 + y^2} < r_N \quad \text{and} \quad 0 \text{ fm} < z < 2r_N/W \text{ fm} \\ -0.99c & \text{if} \quad \sqrt{(x+b)^2 + y^2} < r_N \quad \text{and} \quad -2r_N/W \text{ fm} < z < 0 \text{ fm} \end{cases}$$

The boundaries in z were taken considering the Lorentz contraction of the incident pulse in such a way that at $t = 0$, both pulses are positioned at the center of z.

Estimating the center-of-mass energy per nucleon from the initial pulse velocity is possible. Let's calculate the kinetic energy of a nucleon with mass $m_N \sim 0.9383$ GeV/c^2:

$$E_K = m_N c^2 (W - 1)$$

where W is the Lorentz factor, then each flow initially carries $W = 1/\sqrt{1 - (\frac{0.99c}{c})^2} \sim 7.088$, making a direct substitution in the equation above, we find that

$$E_K \sim 5.712 \text{ GeV}$$

Now, in head-on heavy-ion collisions with identical particles and equal momentum, the center-of-mass energy (COM) is easily computed as:

$$\sqrt{s_{NN}} = 2E_K$$

Therefore, the COM per nucleon in this simulation is estimated to be around $\sqrt{s_{NN}} = 11.4$

A simulation with $r_N = 6.38$ fm, the same radius as a gold nucleus, and an impact parameter $b = 6.38$ fm was initialized to test the previous implementation. The evolution of ρ from t_0 to t_f is shown in the following 3D display

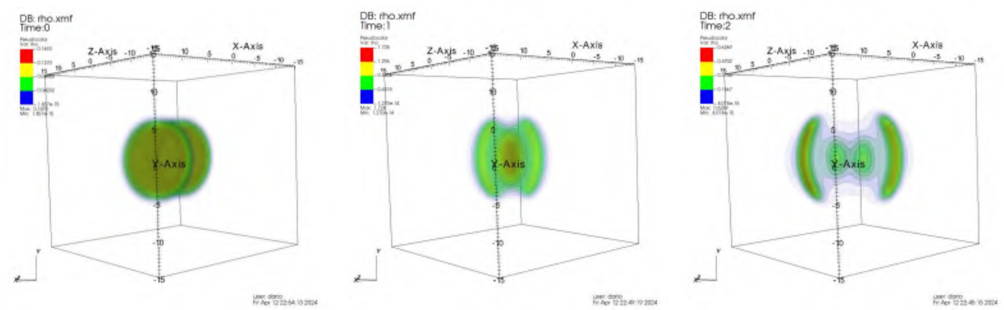

Figure 9: Rest mass density evolution in the 3D shock-shock simulation in a domain defined by $[-15 \text{ fm}, \ 15 \text{ fm}] \times [-15 \text{ fm}, \ 15 \text{ fm}]$. From left to right, the snapshots correspond to times $t = 0$ fm/c, $t = 2.95$ fm/c, $t = 5.3$ fm/c)

As seen, the test showed a successful implementation. Further tests with greater velocities, equivalent to $\sqrt{s_{NN}} = 200$ GeV were intended to be initialized, but so far, the code showed a limitation in the initial velocities in this particular 3D implementation. Nevertheless, three particular simulations exploring head-on, peripheral, and ultra-peripheral collisions, with impact parameters of $b = 0.0$ fm, $b = 6.38$ fm and $b = 12.76$ fm respectively, were made to compare with a more sophisticated model in the next subsection.

3.2 Monte-Carlo Glauber initial conditions

To include nucleon-nucleon interactions, implementing MC-Glauber initial conditions before the hydrodynamical evolution is a good approach. This model arises to solve the problem of scattering of composite particles such as nuclei, and in particular, to compute geometric quantities such as the impact parameter, number of binary collisions, and number of participants. The basic idea is to take a random sample of nucleons over the wood-saxon distribution for two nuclei A and B; with this configuration, we obtain an arrangement of two colliding nuclei in the domain with given parameters that characterize the nature of the collision. The nucleons are labeled with the indexes i and j, and the interaction between them is given if the condition $(x_i - x_j)^2 + (y_i + y_j)^2 < \sigma_{NN}/\pi$ is fulfilled. To obtain an initial state within the Monte Carlo Glauber model and perform the hydrodynamic evolution, we need to translate the positions of the participant nucleons into an initial energy density profile along the transverse plane at the initial time τ_0, given by a Gaussian distribution with a σ smearing. The sum of each Gaussian distribution, either is a participant nucleon or the total number of binary collisions, is what determines the initial state of the system:

$$\epsilon(\tau_0, \vec{x}) = \frac{K}{2\pi\sigma}\{(1-\alpha)\sum_{i=1}^{N_{part}} \exp[-\frac{(\vec{x}-\vec{x}_i^{part})^2}{2\sigma^2}] + \alpha\sum_{i=1}^{N_{coll}} \exp[-\frac{(\vec{x}-\vec{x}_i^{coll})^2}{2\sigma^2}]\} \quad (28)$$

later is multiplied by a piece-wise function involving the rapidity of each energy density contribution and the beam rapidity:

$$f(\eta) = \begin{cases} 0, & |\eta| \geq Y_{beam} \\ \exp\left[-\frac{-\hat{\eta}^2}{2\sigma_\eta}^2\right] & \eta_{flat} \leq |\eta| < Y_{beam} \\ 1, & |\eta| < \eta_{flat} \end{cases} \quad (29)$$

where $\hat{\eta} = |\eta| - \eta_{flat}/2$, and $Y_{beam} = \log \frac{\sqrt{s_{NN}}}{m_N}$.

To have a better understanding of the parameters of this implementation, it's important to emphasize that the parametrization of equations 28 and 29, involving the quantities

η_{flat}, σ_η, σ, K and α, is chosen to reproduce specific experimental results [12], therefore, great part of this setting arises from semi-empirical models. In particular, K is a normalization parameter fixed to reproduce multiplicity results from RHIC experiments. At the same time, α is the hardness fraction, such that $\alpha = 0$ would lead to low-momentum transfer interactions, in which soft scattering between nucleons occurs. On the other hand, equation 29 displays a limit of the energy density profile in the longitudinal direction, particularly achieving full density at the shifted center given by η_{flat} and gradually fading by a Gaussian distribution with smearing σ_η until it reaches 0 at the beam rapidity. Given that m_N is a fixed value, it is worth noting that the larger $\sqrt{s_{NN}}$, the initial energy density distribution becomes longer, as seen in Fig. 11. An important observation is t,hat unlike the simplified model in subsection 12, this MC-Glauber initialization only takes part in the colliding area, ignoring all kinds contributionsion coming from the spectator fraction of the nucleus.

Instead of implementing the MC-Glauber model inside the hydro code, the initialization was imported from an external hydrodynamical code for heavy-ion collisions called ECHO-QGP [11]. Given a domain of the same size, it is possible to interpolate data from the external code and run a simulation with the formalism seen in chapter 2 using CAFE.

For its simplicity, the Lagrange polynomial interpolation was used to approximate the initial conditions from the MC-Glauber model to the initial values in the hydrodynamic Euler equations. The main idea is to perform a quadratic interpolation in each direction, taking 3D cells every three steps in x, y, and z-directions over the domain, in other words, to subdivide the domain into cubic cells of $3 \times 3 \times 3$ nodes each.

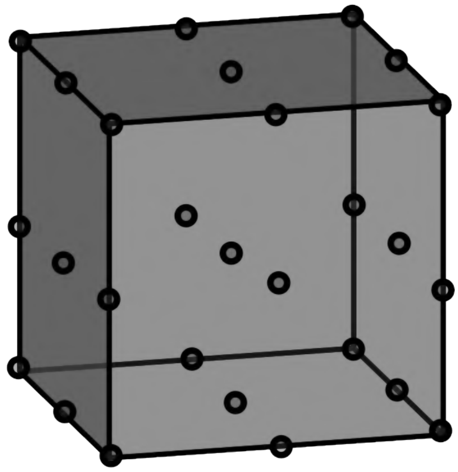

Figure 10: Three-dimensional interpolation cell with 27 nodes. Each node is associated with a value of f, the finality of this proceeding is to approximate additional values of f between nodes.

The generalization for a 3D Lagrange polynomial interpolation reads:

$$f(x, y, z) \approx \sum_{i=1}^{N} f_i(x, y, z) L_i(x, y, z) \tag{30}$$

where

$$L_i(x, y, z) = \prod_{k=1, k \neq i}^{N} \left(\frac{x - x_k}{x_i - x_k} \right) \left(\frac{y - y_k}{y_i - y_k} \right) \left(\frac{z - z_k}{z_i - z_k} \right) \tag{31}$$

It is possible to perform this algorithm recursively in the y and z directions to obtain the approximation given in equation 30, using the previous interpolated function as the input data. The pseudo-code for the One-dimensional Lagrange polynomial, which represents the first iteration in the three-dimensional case, is represented in the box bellow:

Algorithm 1: One dimensional Lagrange polynomial interpolation

Data: $[(x_1, f_1), ..., (x_n, f_n)]$, point

; /* polynomial */

Result: $f_{\text{point}} = \sum_{i=1}^{n} f_i(x) \prod_{k=1,k\neq i}^{n} \left(\frac{\text{point}-x_k}{x_i-x_k}\right)$

$f_{\text{point}} \leftarrow 0$;

$l_i \leftarrow 1$;

for $i = 1$ *to* n **do**

    if *point* $\neq x_i$ **then**

        for $k = 1$ *to* n **do**

            if $i \neq k$ **then**

                $l_i = l_i * \frac{\text{point}-x_k}{x_i-x_k}$

            end

        end

        $f_{\text{point}} = f_{\text{point}} + f_i * l_i$

    else

        $f_{\text{point}} = f_i$

    end

end

The previous steps may be used to develop the generalized 3D case. In this work, the interpolation was issued as a complementary tool in the enhanced version of the CAFE code.

Going back to the Monte-Carlo conditions in ECHO-QGP, we obtained different samples of data from Au+Au simulations at energies of 11.4 GeV, 200 GeV, and 2.7 TeV, to test the hydrodynamic model at low, intermediate, and high energies respectively. The following figures show the 3D display from the MC-Glauber initial conditions at $t = 0.59$ fm/c after the collision.

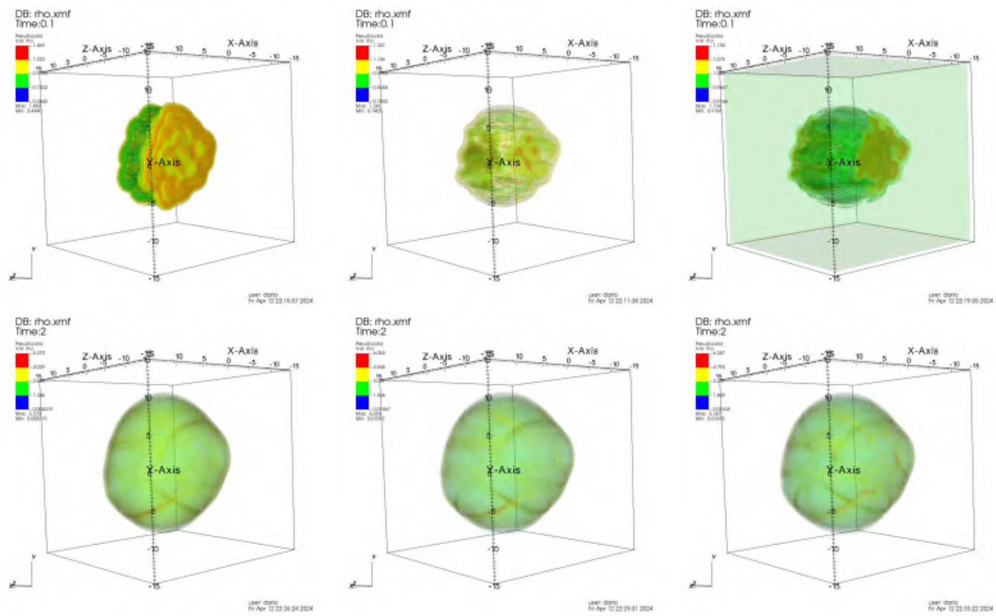

Figure 11: Rest mass density evolution in with the MC-Glauber initial data over a domain defined by $[-15 \text{ fm}, \ 15 \text{ fm}] \times [-15 \text{ fm}, \ 15 \text{ fm}]$. The snapshots from left to right correspond to beam energies of 11.4 GeV, 200 GeV and 2.7 TeV. The snapshots on the top correspond to $t = 0.59$ fm/c, while the ones on the bottom correspond to the final time $t = 5.9$ fm/c

4 Chapter III: Results

In this section, we analyze the results obtained after a series of simulations, either using internal configurations in CAFE or interpolating initial data from ECHO-QGP. In the following table, the basic configurations for a total of thirteen simulations are synthesized:

$\sqrt{s_{NN}}$	Model	Nucleus type	Impact parameter
11.4 GeV	MC-Glauber	Au+Au	$b = 11.90$ fm, 2.92 fm
	Simplified	Au+Au	$b = 0$ fm, 6.38 fm, 12.76 fm
200 GeV	MC-Glauber	Au+Au	$b = 11.90$ fm, 2.92 fm, 10.83 fm, 5.88 fm
2.7 TeV	MC-Glauber	Au+Au	$b = 11.90$ fm, 2.92 fm
	MC-Glauber	Pb+Pb	$b = 11.90$ fm, 2.92 fm

For the simplified model in section 3.1, three main simulations were executed with different impact parameters of $b = 0$ fm, 6.38 fm, and 12.76 fm, for head-on, semi-central, and peripheral events respectively, with $r_N = 6.38$ fm corresponding to the gold (Au) nuclear radius. On the other hand, for the MC-Glauber simulations, the previous value for Au was used, and $r_N = 6.66$ fm corresponds to the lead (Pb) nuclear radius. The following figure shows the temperature distribution in the transverse plane, where each column represents a different impact parameter and each row has a different evolution time.

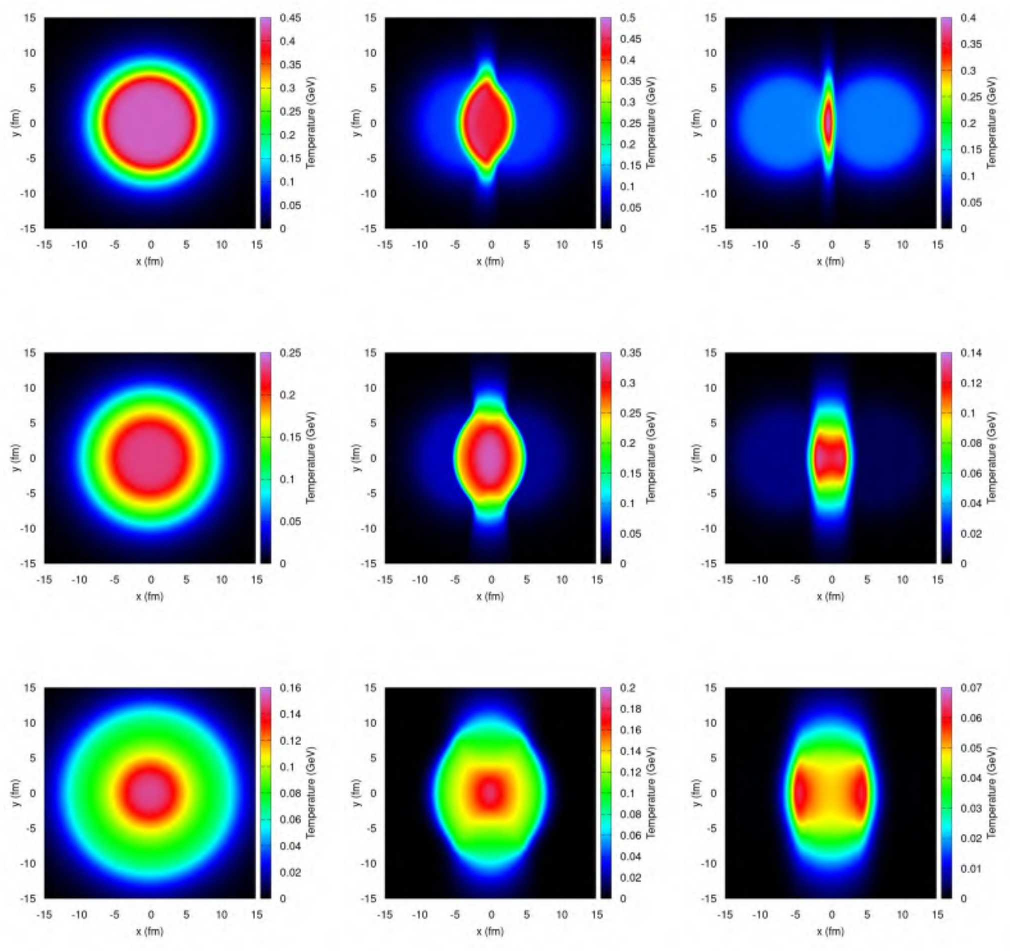

Figure 12: Temperature distributions in the macroscopic approach. The snapshots from top to bottom correspond to times $t = 0.59$ fm/c, $t = 2.95$ fm/c and final time $t = 5.3$ fm/c. From left to right, correspond to impact parameters $b = 0$ fm, $b = 6.38$ fm and $b = 12.76$ fm

The first thing to note comparing temperatures in fig 12 is that the temperatures in all snapshots in the event with $b = 6.38$ fm appear to be higher than those in the head-on collision. Also, the peripheral event shows considerable high temperatures, even with the peripheral nature of the collision; this result is inconsistent with empirical result, since lower centralities (short impact parameters) are related to higher particle production, and greater temperatures are inferred from the latter. Given the simplicity of this model, further simulations including nucleon-nucleon fluctuations must be analyzed and compared with the ones in this section.

The next two simulations were executed using MC-Glauber initial conditions in an attempt to emulate the previous scenario of Au+Au collisions, in this case with a center of mass energy of $\sqrt{s_{NN}} = 200$ GeV. One disadvantage of using the MC-Glauber model is that the random samples lead to random impact parameters, therefore having limited control over this initial data. Nevertheless, real heavy-ion collision experiments lack this control as well, therefore in the case of these simulations, further analyses can be done relying on statistics. The impact parameters for this simulations were $b = 2.92$ fm and $b = 11.90$ fm:

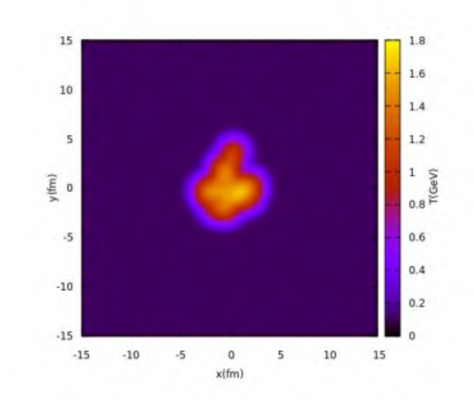

Figure 13: Pressure distribution in the transverse plane at a proper time $\tau = 0.0$ fm$/c$ with an impact parameter of $b = 11.90$ fm.

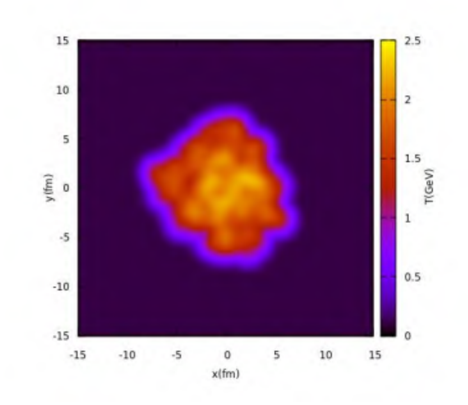

Figure 14: Pressure distribution in the transverse plane at a proper time $\tau = 0.0$ fm$/c$ with an impact parameter of $b = 2.92$ fm.

Making a comparison between Figures 13 and 14, we can see that by adding nucleon-nucleon interactions in the initial conditions, the maximum temperature increases the more central the collisions are. However, the temperatures at initial times still surpass the results using only ECHO-QGP for the two initial conditions and hydrodynamic evolution, as the maximum temperature is still around a few GeV. A review of the simulations executed so far is needed to continue with the project and obtain consistent results.

Nevertheless, it is worth making a general analysis of the temperature evolution over time, to do this the *Query* tool in the Visit 3D viewer was used to summarize the data for each simulation. For each temperature distribution over time, three metrics: the maximum, average, and minimum values, were considered. The first may suggest that conditions for QGP production were reached at some point during the simulation; on the other hand, the average value may show better accuracy for experimental results given that it projects a collective behavior, and also makes a basis for a general thermal profile; finally, the minimum value evolution makes possible to estimate a range of time in which the cooling phase makes the hydrodynamical description non-viable (potential hadronization), and in the best of cases, encourage a search for a more plausible system description. The following figures correspond to the results of the simplified model previously proposed:

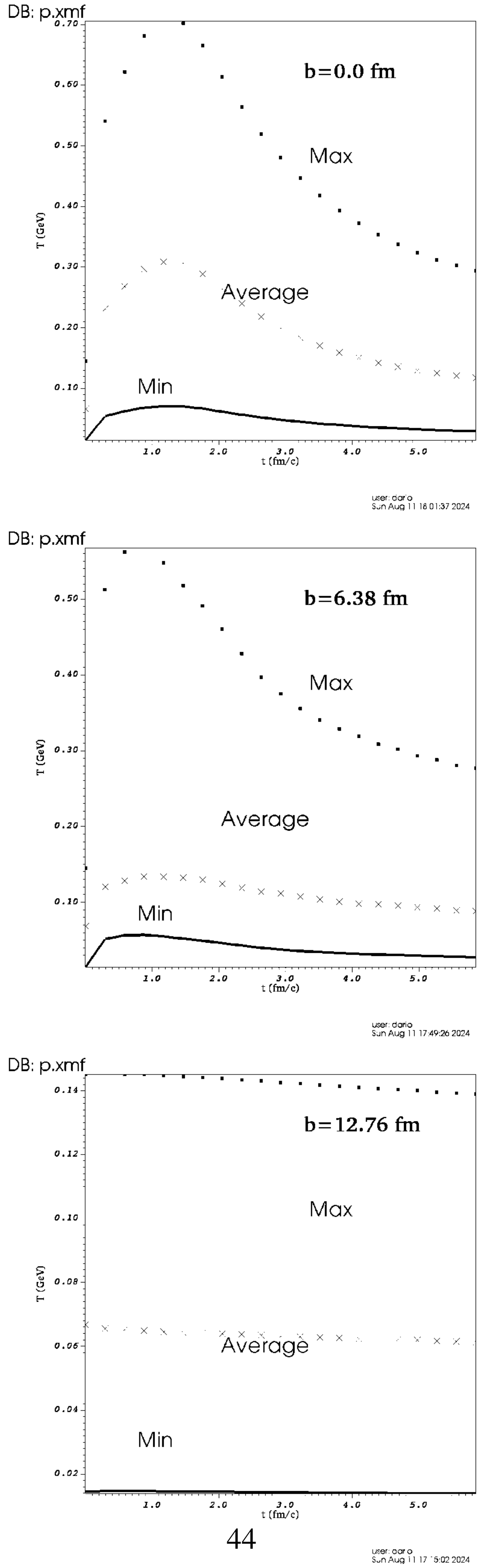

Figure 15: Thermal evolution over time for central (top), semi-central, and peripheral (bottom) simulations using the simplified approach. The peripheral case shows temperature ranges that make a possible QGP formation implausible.

In the first two distributions testing the simplified model, is is possible to observe a peak in the temperature around $\tau = 1$ fm/C, which just reflects that at initial time, the currents haven't interacted with each other. In the last distribution, that peak is not present because neither of these currents have direct contact, moreover, the maximum profile represented by dotted squares, seem to reach temperatures needed for QGP formation, although ultra-peripheral events have little chance to evolve for this to happen as interaction is very limited.

In the case of the MC-Glauber simulations, the most extreme impact parameter events were shown, that is, events with $b = 2.92$ fm (almost central) and $b = 11.90$ fm (nearly peripheral). We took three collision energies to evaluate conditions similar to the data obtained in RHIC (Au+Au at 200 GeV) and CERN (Pb+Pb at 2.7 TeV) facilities, with an attempt to approach these results to some degree; for the case of the simulation with $\sqrt{s_{NN}} = 11.4$ GeV, so far there's not enough experimental data available to compare with the simulations. Therefore, only general speculations about the results can be made. The following thermal profiles project the previous insight; each column shows a different beam energy, and each row shows one extreme of the impact parameter case. In figure 16, the average profile in the first row, representing events at $\sqrt{s_{NN}}$ =11.4 GeV, show values that surpass the empirical profiles with 200 GeV at RHIC.

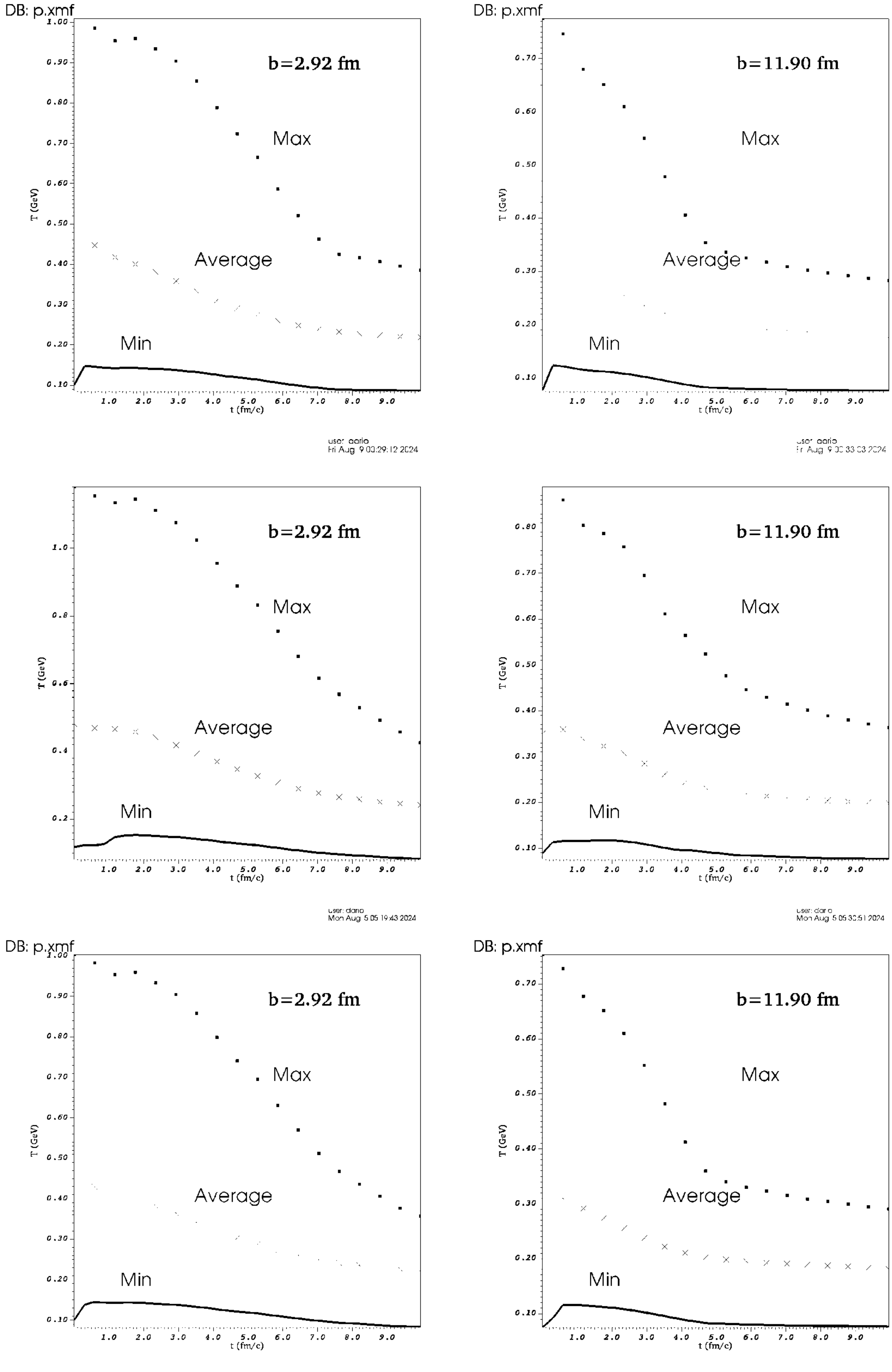

Figure 16: Thermal evolution over time for the MC-Glauber simulations. Each row correspond to the beam energies of $\sqrt{s_{NN}} = 11.4$ GeV, 200 GeV and 2.7 TeV. On the other hand, each column represents the simulations with $b = 2.92$ fm and $b = 11.90$ fm

The final query was made to compare the evolution of temperature at energies of 200 GeV, in an attempt to reproduce experimental thermal profiles obtained at RHIC with different centralities. For this particular case, a total of four impact parameters were taken.

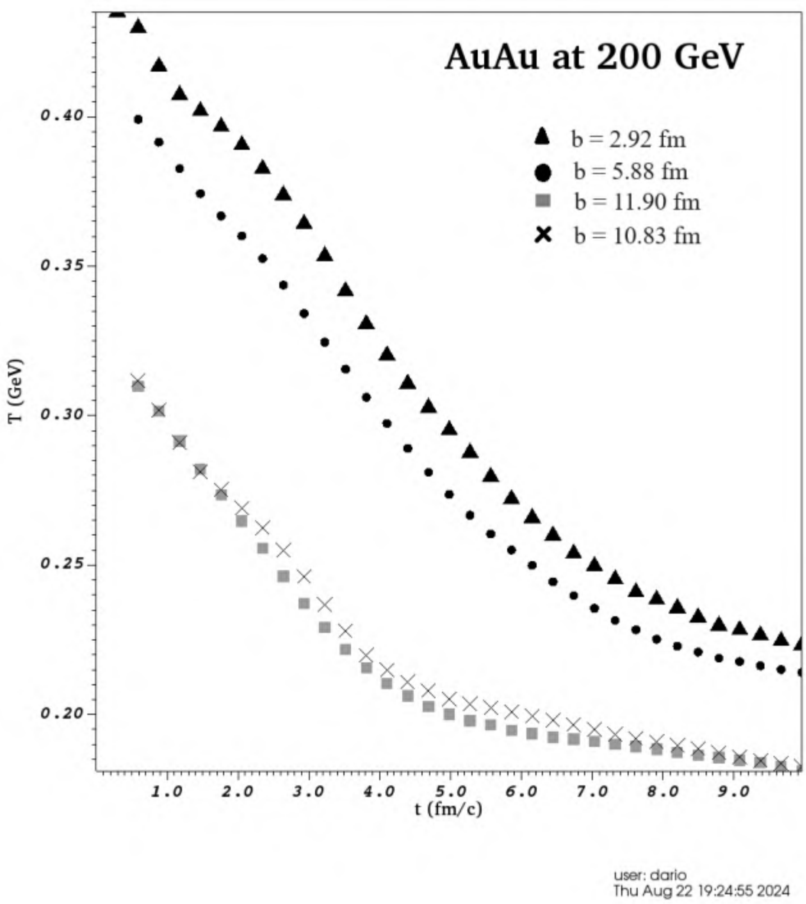

Figure 17: Average temperature evolution for semi-central events from $t = 0$ fm/c to $t = 10$ fm/c. Four impact parameters were tested, showing a slow cooling behavior after a certain time.

It is possible to perceive that the thermal profiles coincide with the main idea that the greater the impact parameter, the lower the temperature and the lower the chances of producing conditions for QGP formation. Nevertheless, overall behaviour and initial temperatures at either impact parameter are similar or surpass the ones obtained at the center of the fireball in more sophisticated models and analytic solution for the temperature in function of the proper time τ. [11] [13]

5 Chapter IV: Conclusions

As seen in chapter 3 is that the simplified approach has considerable limitations; specifically, the code breaks with initial velocities equivalent to events at $\sqrt{s_{NN}} = 200$ GeV, making it only possible to be tested with low energies. The principal disadvantage of this limitation is that the data from heavy-ion collision experiments at low energies is limited, making it hard to make parametrizations to reproduce experimental results as seen at the beginning of chapter 4. Furthermore, the simplicity of this model leads to inconsistent results, most likely due the uniformity of the initial mass density profile, and also due the query taking areas in the peripheries that don't interact and just continue to move in the beam direction, adding noise to the computing.

In the case of the MC-Glauber tests, simulations at 11.4 GeV were performed without sufficient data to parameterized the initial energy density profile, therefore, inaccuracy in those results were expected. As for the cases of 200 GeV and 2.7 TeV, both groups of simulations show greater temperatures that the ones registered in the state of the art.

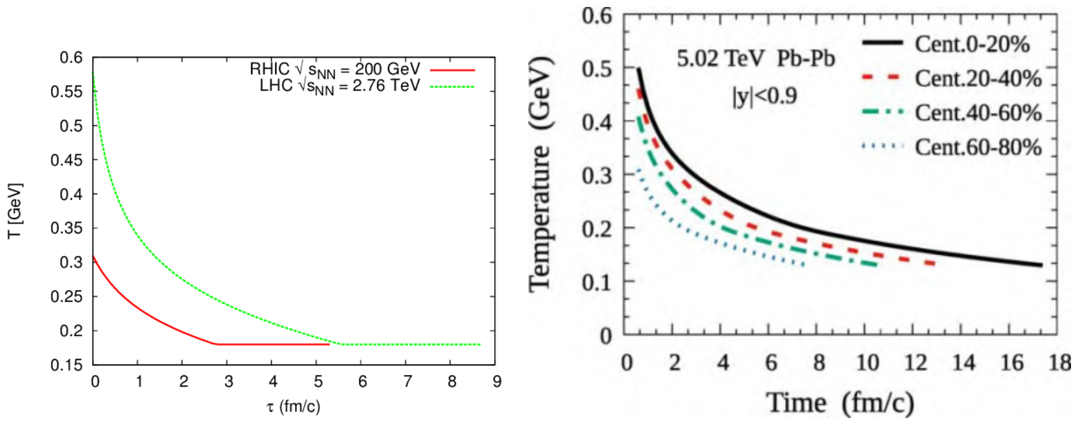

Figure 18: Tempreature profiles obtained from Ralph Rapp [14] (left), and Baoyi Chen et al [13] (right).

Both of the previous figures were taken at the center of the fireball, were the temperature reaches its maximum values. In particular, the temperature profiles with $\sqrt{s_{NN}} = 5$ TeV, show different distributions depending on its centralities, if we compare them with the ones in figure 17 at 200 GeV, we can see that the simulations made with the tools described in this work show, overall, temperatures that exceed the ones with more complex and accurate tools, and most importantly, with empirical results obtained directly from facilities. The tools in this text that describe the evolution of thermodynamic properties were: the ideal gas and Euler equations of hydrodynamics. Both of them show great utility at introductory level, for their simplicity and descriptive accuracy less complex systems. It is important to emphasize that this work used ideal hydrodynamics as its main work-frame to describe a fundamentally microscopic picture, it was intended to test its limitations in events where there is an intersection of microscopic and macroscopic dynamics.

Three main paths of work can be taken here to make improvements in further research: include viscous hydrodynamics, QCD equations of state and implement the hadronization phase description. The great temperatures reached in the simulations may come from the non-viscous evolution, thus suppressing energy dissipation internally because the limited interaction inside the medium; with this in mind, the next step in complexity could be implementing the Navier-Stokes equations of viscous hydrodynamics. The ideal gas equation of state adds limitations to the thermodynamic properties, moreover, it aims to describe a potentially liquid-like medium as a non interacting gas; different energy approaches in QCD have been developed using interesting frameworks for the space-time description (lattice-QCD), making the thermodynamical description more specific for different beam energies. Finally, in experiments, the temperature profile and QGP formation evidence are inferred indirectly by observables akin to particle description such as multiplicity, particle spectra and jet-quenching; these properties can't be obtained solely by hydrodynamics, therefore, adding the Cooper-Frye formula to making a descriptive switch from hydrodynamics to non-zero mass particles (hadronisation phase).

We conclude this text with a philosophical proposal by stating that idealization aims for a raw description of nature, whereas reality not necessarily its subject to it. Furthermore, nature is not subject to improvements, physics work is to describe nature as it comes, either mild or extreme as this scenario. The ideal description is a great introduction to describe simplified scenario, yet it is subject of improvements according to reality and our continuous intention to get a minor glance to what some people call ”the truth”; when someone embrace the ideal, the truth slips through their fingers, paradoxically, when someone embraces the truth, there’s no further work to be done: truth is meant to slip through our fingers, otherwise will be condemned to an unchanged state.

References

[1] W. Busza, K. Rajagopal, and W. van der Schee, "Heavy ion collisions: The big picture and the big questions," *Annual Review of Nuclear and Particle Science*, vol. 68, no. 1, pp. 339–376, oct 2018. [Online]. Available: https://doi.org/10.1146%2Fannurev-nucl-101917-020852

[2] B. McInnes, "A rotation/magnetism analogy for the quark plasma," *Nuclear Physics B*, vol. 911, 04 2016.

[3] A. Margaryan, "Transverse asymmetry in nucleon deuteron scattering in pionless effective field theory," 11 2017.

[4] M. Gyulassy and L. McLerran, "New forms of qcd matter discovered at rhic," *Nuclear Physics A*, vol. 750, no. 1, p. 30–63, Mar. 2005. [Online]. Available: http://dx.doi.org/10.1016/j.nuclphysa.2004.10.034

[5] B. Schenke, S. Jeon, and C. Gale, "(3+1)d hydrodynamic simulation of relativistic heavy-ion collisions," *Physical Review C*, vol. 82, no. 1, jul 2010. [Online]. Available: https://doi.org/10.1103%2Fphysrevc.82.014903

[6] F. D. Lora-Clavijo, A. Cruz-Osorio, and F. S. Guzmá n, "CAFE: A NEW RELATIVISTIC MHD CODE," *The Astrophysical Journal Supplement Series*, vol. 218, no. 2, p. 24, jun 2015. [Online]. Available: https://doi.org/10.1088%2F0067-0049%2F218%2F2%2F24

[7] L. Rezzolla and O. Zanotti, *Relativistic Hydrodynamics*, ser. EBSCO ebook academic collection. OUP Oxford, 2013. [Online]. Available: https://books.google.com.mx/books?id=KU2oAAAAQBAJ

[8] M. Alcubierre, *Introduction to 3+1 Numerical Relativity*, ser. International Series of Monographs on Physics. OUP Oxford, 2008. [Online]. Available: https://books.google.com.mx/books?id=4hDvRvVJeEIC

[9] J. W. Harris and B. Müller, "The search for the quark-gluon plasma," *Annual Review of Nuclear and Particle Science*, vol. 46, no. 1, pp. 71–107, 1996.

[10] M. Göckeler, R. Horsley, A. C. Irving, D. Pleiter, P. E. L. Rakow, G. Schierholz, and H. Stüben, "Determination of the lambda parameter from full lattice qcd," *Phys. Rev. D*, vol. 73, Jan 2006. [Online]. Available: https://link.aps.org/doi/10.1103/PhysRevD.73.014513

[11] L. Del Zanna, V. Chandra, G. Inghirami, V. Rolando, A. Beraudo, A. De Pace, G. Pagliara, A. Drago, and F. Becattini, "Relativistic viscous hydrodynamics for heavy-ion collisions with echo-qgp," *The European Physical Journal C*, vol. 73, no. 8, Aug. 2013. [Online]. Available: http://dx.doi.org/10.1140/epjc/s10052-013-2524-5

[12] T. Hirano, P. Huovinen, K. Murase, and Y. Nara, "Integrated dynamical approach to relativistic heavy ion collisions," *Progress in Particle and Nuclear Physics*, vol. 70, pp. 108–158, 2013. [Online]. Available: https://www.sciencedirect.com/science/article/pii/S0146641013000045

[13] B. Chen, L. Jiang, X.-H. Liu, Y. Liu, and J. Zhao, "$x(3872)$ production in relativistic heavy-ion collisions," *Phys. Rev. C*, vol. 105, p. 054901, May 2022. [Online]. Available: https://link.aps.org/doi/10.1103/PhysRevC.105.054901

[14] R. Rapp, "Dilepton spectroscopy of qcd matter at collider energies," *Advances in High Energy Physics*, vol. 2013, 01 2013.

Darío Chaires Arciniega

Temperature analysis of hadronic current simulations using relativistic hydrodynamics for heavy-ion collisions scenarios.p...

Universidad Michoacana de San Nicolás de Hidalgo

Detalles del documento

Identificador de la entrega

trn:oid:::3117:512273059

Fecha de entrega

13 oct 2025, 7:46 a.m. GMT-6

Fecha de descarga

13 oct 2025, 7:48 a.m. GMT-6

Nombre del archivo

Temperature analysis of hadronic current simulations using relativistic hydrodynamics for heavy....pdf

Tamaño del archivo

5.1 MB

53 páginas

9447 palabras

45.227 caracteres

18% Similitud general

El total combinado de todas las coincidencias, incluidas las fuentes superpuestas, para ca...

Grupos de coincidencias

- **144** Sin cita o referencia 18%
  Coincidencias sin una citación ni comillas en el texto
- **2** Faltan citas 0%
  Coincidencias que siguen siendo muy similar al material fuente
- **2** Falta referencia 0%
  Las coincidencias tienen comillas, pero no una citación correcta en el texto
- **0** Con comillas y referencia 0%
  Coincidencias de citación en el texto, pero sin comillas

Fuentes principales

15% Fuentes de Internet
15% Publicaciones
0% Trabajos entregados (trabajos del estudiante)

Marcas de integridad

N.º de alerta de integridad para revisión

Caracteres reemplazados
89 caracteres sospechosos en N.º de páginas
Las letras son intercambiadas por caracteres similares de otro alfabeto.

Los algoritmos de nuestro sistema analizan un documento en profundidad para buscar inconsistencias que permitirían distinguirlo de una entrega normal. Si advertimos algo extraño, lo marcamos como una alerta para que pueda revisarlo.

Una marca de alerta no es necesariamente un indicador de problemas. Sin embargo, recomendamos que preste atención y la revise.

Formato de Declaración de Originalidad y Uso de Inteligencia Artificial

Coordinación General de Estudios de Posgrado
Universidad Michoacana de San Nicolás de Hidalgo

CGEP UMSNH

A quien corresponda,

Por este medio, quien abajo firma, bajo protesta de decir verdad, declara lo siguiente:

- Que presenta para revisión de originalidad el manuscrito cuyos detalles se especifican abajo.
- Que todas las fuentes consultadas para la elaboración del manuscrito están debidamente identificadas dentro del cuerpo del texto, e incluidas en la lista de referencias.
- Que, en caso de haber usado un sistema de inteligencia artificial, en cualquier etapa del desarrollo de su trabajo, lo ha especificado en la tabla que se encuentra en este documento.
- Que conoce la normativa de la Universidad Michoacana de San Nicolás de Hidalgo, en particular los Incisos IX y XII del artículo 85, y los artículos 88 y 101 del Estatuto Universitario de la UMSNH, además del transitorio tercero del Reglamento General para los Estudios de Posgrado de la UMSNH.

Datos del manuscrito que se presenta a revisión		
Programa educativo	Maestría enciencias en Ingeniería Física	
Título del trabajo	Temperature analysis of hadronic current simulations using relativistic hydrodynamics for heavy-ion collisions scenarios	
	Nombre	**Correo electrónico**
Autor/es	Darío Chaires Arciniega	2132224a@umich.mx
Director	Francisco Shidartha Guzmán Murillo	francisco.s.guzman@umich.mx
Codirector		
Coordinador del programa	Dagoberto Cardona Ramírez	dagoberto.cardona@umich.mx

Uso de Inteligencia Artificial		
Rubro	**Uso (sí/no)**	**Descripción**
Asistencia en la redacción	sí	Para mejorar el entendimiento y hacer más conciso el texto, uso sólo de referencia

Formato de Declaración de Originalidad y Uso de Inteligencia Artificial

Coordinación General de Estudios de Posgrado
Universidad Michoacana de San Nicolás de Hidalgo

Uso de Inteligencia Artificial		
Rubro	**Uso (sí/no)**	**Descripción**
Traducción al español	No	
Traducción a otra lengua	Sí	Mejorar la redacción de algunas líneas
Revisión y corrección de estilo	No	
Análisis de datos	NO	
Búsqueda y organización de información	NO	
Formateo de las referencias bibliográficas	NO	
Generación de contenido multimedia	NO	
Otro	NO	

Datos del solicitante	
Nombre y firma	
Lugar y fecha	Morelia, Michoacán. 8 de Octubre del 2025